Global bifurcation structure of a four-dimensional Lorenz-like system with a wild chaotic attractor

Juan Patiño-Echeverría, Bernd Krauskopf and Hinke M. Osinga
Department of Mathematics, University of Auckland, New Zealand

June 2025

Abstract

Wild chaos is a higher-dimensional form of chaotic dynamics that can only arise in vector fields of dimension at least four. It is characterized by the persistent presence of tangencies between stable and unstable manifolds of an invariant set. We study a four-dimensional extension of the classic Lorenz system, which was recently shown to exhibit a so-called wild pseudohyperbolic attractor for a specific choice of parameters. Pseudohyperbolicity guarantees that every trajectory in the attractor has a positive maximal Lyapunov exponent, and this property persists under small perturbations of the system.

We investigate how wild chaotic attractors arise geometrically by analysing the overall bifurcation structure in the (ρ, μ)-plane. Here, ρ is the standard (Rayleigh) parameter in the classic Lorenz system, and μ is a new parameter that introduces spiralling dynamics near the origin. We begin by identifying the bifurcation structure inherited from the Lorenz system by continuing its homoclinic bifurcations as curves. Kneading diagrams, in combination with Lin's method, allow us to uncover additional curves of global bifurcation intrinsic to the four-dimensional system. We also compute the Lyapunov spectrum of the unstable manifold of the origin to identify different types of attractors. This approach provides insight into the parameter regions where wild chaos may occur.

1 Introduction

We study a four-dimensional extension of the classic Lorenz system [35] as proposed in [40]:

$$\left\{ \begin{array}{rcl} \dot{x} & = & \sigma\,(y - x), \\ \dot{y} & = & x\,(\rho - z) - y, \\ \dot{z} & = & x\,y - \beta\,z + \mu\,w, \\ \dot{w} & = & -\mu\,z - \beta w, \end{array} \right. \tag{1}$$

where σ, β, ρ, and μ are non-negative parameters. As is standard in the field, we fix the parameters $\sigma = 10$ and $\beta = 8/3$ throughout this paper. When $\mu = 0$, the hyperplane $\{w = 0\}$ is invariant, and system (1) restricted to this hyperplane is the three-dimensional Lorenz system. Indeed, many properties of the classic Lorenz system carry over to the four-dimensional system (1). In particular, system (1) exhibits a rotational symmetry given by $(x, y, z, w) \mapsto (-x, -y, z, w)$, and its divergence is $-(2\beta + \sigma + 1) < 0$, so that system (1) is dissipative. Furthermore, the origin $\mathbf{0}$ is always an equilibrium that coexist, for $\rho > 1$, with a pair of rotationally symmetric equilibria

$$p^{\pm} := \left(\pm\sqrt{\frac{(\rho-1)(\beta^2+\mu^2)}{\beta}}, \pm\sqrt{\frac{(\rho-1)(\beta^2+\mu^2)}{\beta}}, \rho - 1, \frac{-\mu\,(\rho-1)}{\beta} \right).$$

System (1) was proposed in [40] as a candidate for a vector field exhibiting a *wild* spiral chaotic attractor. Here, *wild* refers to the fact that the existence of homoclinic tangencies is structurally stable in the C^1-topology. In other words, any sufficiently small C^1-perturbation of the system will also have a chaotic attractor with a homoclinic tangency [37, 9, 43, 44]. The notion of wild chaotic sets goes back to Newhouse, who showed that, in the C^2-topology, planar diffeomorphisms can have robust homoclinic tangencies [36]. For C^1-robustness of homoclinic tangencies, a three-dimensional diffeomorphism, or equivalently, a four-dimensional vector field is required; see [22, 43, 45] for background and theory.

System (1) is among the few examples currently known of higher-dimensional vector fields that exhibit wild chaotic attractors. The important new ingredient is that for $\mu > 0$ and $\rho > 1$, the origin is a saddle-focus equilibrium, unlike in the Lorenz system, where the origin is a saddle with real eigenvalues. This means that in (1), all homoclinic orbits when $\mu > 0$ and $\rho > 1$ are of Shilnikov type. Recently, Gonchenko, Kazakov, and Turaev [23] introduced a numerical technique to determine whether an attractor is *pseudohyperbolic* by computing Lyapunov exponents and their associated eigenfunctions. Pseudohyperbolicity is a key property that ensures the robustness of chaotic dynamics and the absence of *periodic windows*; see again [22, 43, 45]. Using this technique and the computation of kneading diagrams [6] in the (ρ, σ)-plane, they showed numerically that system (1) has a wild pseudohyperbolic chaotic attractor for the standard values of σ and β, with $\rho = 25$ and $\mu = 7$.

To set the stage, Fig. 1 shows the three saddle-focus equilibria $\mathbf{0}$ and $p^{\pm}$ of system (1) at the parameter point $(\rho, \mu) = (25, 7)$, which we will refer as (ρ^*, μ^*) throughout this paper. Also shown is the one-dimensional unstable manifold $W^u(\mathbf{0})$ of $\mathbf{0}$ (consisting of trajectories that converge to $\mathbf{0}$ in backward time), which accumulates on the attractor; see also [23, Fig. 1]. Panel (a) is a projection onto (x, y, z)-space, and panels (b) and (c) show projections onto (x, y, w)-space and (x, z, w)-space, respectively. Notice the rotational symmetry of system (1). The value $\rho = 25$ chosen in [23] is slightly smaller than the standard value $\rho = 28$ associated with the classic chaotic attractor in the Lorenz system [35, 41, 2, 42]. The results in [23] establish a connection between the theoretical framework of wild chaotic attractors developed in [44, 43] and numerical evidence for their existence in this specific four-dimensional system. However, there is as yet no description of the bifurcation structure of system (1) or the precise transitions to or from a wild chaotic attractor.

Here, we carry out a two-parameter bifurcation analysis of system (1) to understand the geometric structures in the (ρ, μ)-plane that give rise to different attractors and, in particular, to a wild chaotic attractor as that in Fig. 1. Specifically, we investigate the backbone structure of system (1), consisting of equilibria and periodic orbits, together with their associated stable and unstable manifolds. Our goal is to identify (sequences of) global bifurcations responsible for creating wild attractors as parameters vary. Specifically, we address the following key questions:

- How do the bifurcations of the classic Lorenz system extend into the two-parameter (ρ, μ)-plane?
- What is the overall global structure of the bifurcation curves in the (ρ, μ)-plane?
- What types of attractors exist in system (1), and under what conditions does a wild chaotic attractor arise?
- What bifurcation mechanisms lead to the emergence of wild chaos?

To answer these questions, we begin by considering global bifurcations of the classic Lorenz system that were identified in [15] and continue them as curves in the (ρ, μ)-plane of system (1), which we achieve with the package `AUTO` [13, 14]. This first step allows us to understand the organization of bifurcations inherited from the Lorenz system, revealing a complicated structure of global bifurcations. The bifurcation diagram highlights the primary homoclinic bifurcation curve as an upper boundary for the other global bifurcations. This curve emerges from the

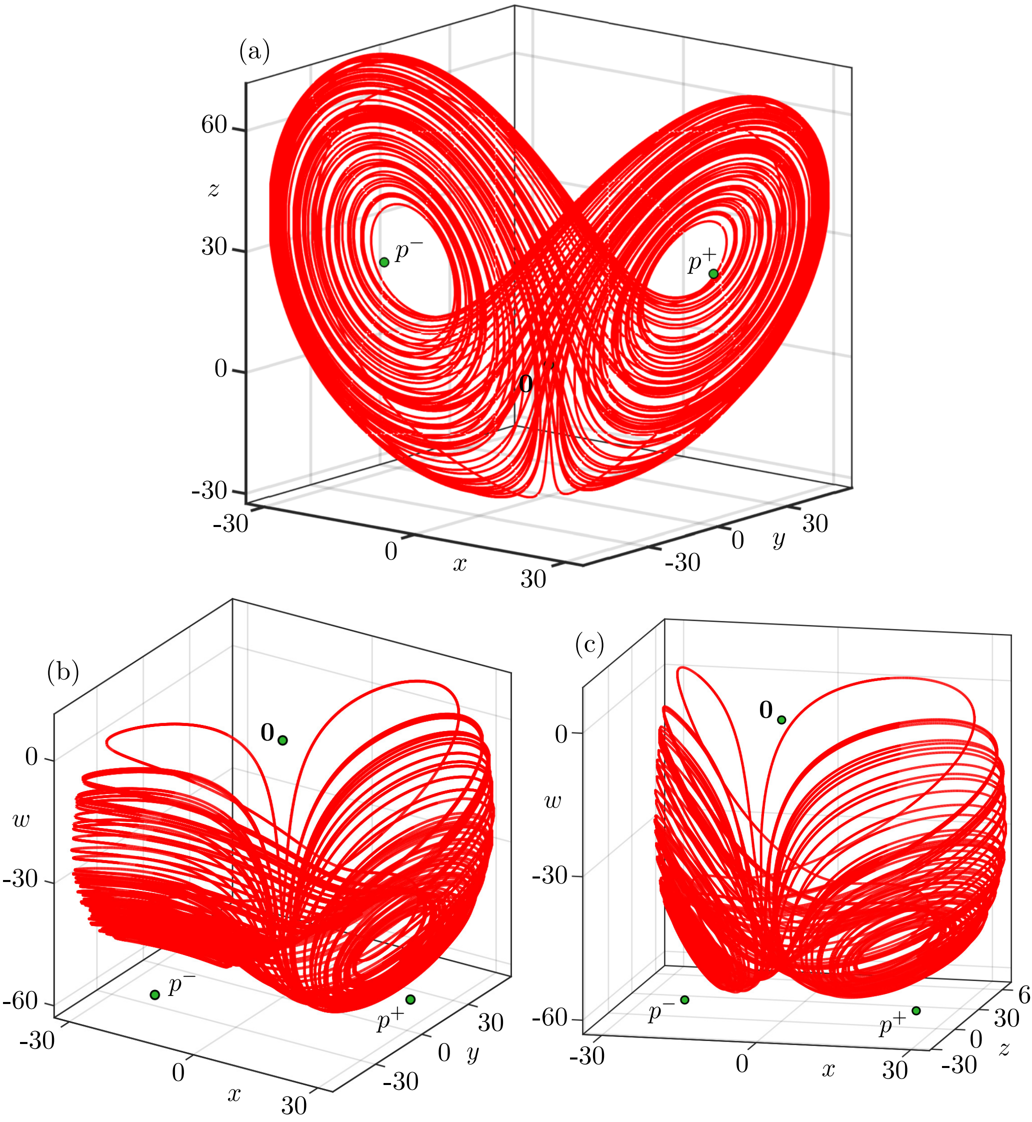

Figure 1: The attractor of system (1) for $\sigma = 10$, $\rho = 25$, $\beta = 8/3$, and $\mu = 7$, represented by the one-dimensional unstable manifold $W^u(\mathbf{0})$ (red curve) of the saddle equilibrium $\mathbf{0}$ (green dot). Shown are projections onto (x, y, z)-space (a), (x, y, w)-space (b), and (x, z, w)-space (c); also shown are the saddle equilibria $p^{\pm}$ (green dots).

so-called homoclinic explosion point in the Lorenz system [41], which also acts as an organizing centre for the dynamics of system (1) in the (ρ, μ)-plane.

We find that all the bifurcation curves inherited from the Lorenz system lie below the point (ρ^*, μ^*), where the wild chaotic attractor was identified in [23]. However, as the next step, we identify new global bifurcations not present in the Lorenz system. Specifically, homoclinic orbits of the origin in the Lorenz system always make a single 'excursion' around either p^+ or p^- and then are forced to 'visit' the opposite symmetric equilibrium [15]. We find that homoclinic orbits of the four-dimensional system (1) can make multiple 'excursions' around the first equilibrium before 'visiting' the symmetric counterpart. Moreover, all homoclinic orbits to $\mathbf{0}$ in system (1) are of 'chaotic' Shilnikov type because the saddle quantity of $\mathbf{0}$ is always positive [31]. We find many homoclinic orbits with these properties in system (1). Several of them also originate from the homoclinic explosion point on the ρ-axis, despite the fact that they do not exist as actual homoclinic orbits in the classic Lorenz system. To identify and continue this type of homoclinic bifurcations, we employ kneading diagrams [6] combined with Lin's method [29]. This approach reveals the intricate structure of the bifurcations and shows how these curves accumulate densely near the point (ρ^*, μ^*). To study the nature of the attractors in system (1), we also compute the Lyapunov spectrum of $W^u(\mathbf{0})$, which allows us to investigate pseudohyperbolicity by comparing the Lyapunov exponents with the topological information obtained from the bifurcation and kneading diagrams.

This paper is organized as follows. In Se. 2, we present and describe the basic properties and local bifurcation structure of system (1) in the (ρ, μ)-plane. In Se. 3, we study global bifurcations of system (1) that originate from the classic Lorenz system, showing how they are organized as curves in the (ρ, μ)-plane. In Se. 4, we introduce the kneading diagram of $W^u(\mathbf{0})$, which enables the identification of additional curves of secondary homoclinic bifurcation. In Se. 5, we compactify the parameter plane to the (quarter) Poincaré disk, which allows us to visualize the global organization of the bifurcation curves, and in particular, we identify a homoclinic explosion point at infinity as an organizing centre of the dynamics of system (1). The kneading diagram reveals the denseness of homoclinic bifurcations near (ρ^*, μ^*), providing numerical evidence for the wild nature of the chaotic attractor. In Se. 6, we present the associated Lyapunov spectrum of the unstable manifold of the origin to identify different types of attractors. Finally, in Se. 7, we summarize our findings and discuss possible directions for future research.

2 Local and global bifurcations of equilibria and the primary periodic orbits

Figure 2 shows, for three different fixed values of μ, the one-parameter bifurcation diagram of system (1) when varying ρ. The starting point is the case $\mu = 0$ in panel (a) of the classic Lorenz system [35]; we refer to [41, 17, 16, 24, 42] for more details and background of this three-dimensional system. As we already mentioned, $\mathbf{0}$ is always an equilibrium, and its eigenvalues are

$$\lambda_{1,2} = \tfrac{1}{2}(\sigma + 1) \pm \tfrac{1}{2}\sqrt{(\sigma - 1)^2 + 4\,\sigma\rho} \quad \text{and} \quad \lambda_{3,4} = -\beta \pm \mu\, i.$$

Hence, $\mathbf{0}$ is initially stable until it loses stability in a pitchfork bifurcation P at $\rho = 1$; for $\rho > 1$, $\mathbf{0}$ is a real saddle with one unstable and three stable eigenvalues. The symmetric pair of equilibria $p^{\pm}$, born at $\rho = 1$, are initially stable until they lose stability in a subcritical Hopf bifurcation H at $\rho_{\mathrm{H}} \approx 24.7368$. Beyond H, the pair $p^{\pm}$ are saddle foci with two unstable eigenvalues. For values of ρ before ρ_{H}, there exists a pair of saddle periodic orbits $\Gamma^{\pm}$, which have a single unstable Floquet multiplier, meaning that they have three-dimensional stable manifolds $W^s(\Gamma^{\pm})$ (consisting of trajectories that converge to $\Gamma^{\pm}$ in forward time). The pair $\Gamma^{\pm}$ shrink down to $p^{\pm}$ and disappear at H; the branch of periodic orbits is represented in Fig. 2(a) by the maximum and minimum of $|x|$. A pair of homoclinic orbits to $\mathbf{0}$ exists at the codimension-one global bifurcation denoted $\mathrm{Hom}_{\mathtt{r}}$ at $\rho_{\mathtt{r}} \approx 13.9565$. It famously creates, for $\rho > \rho_{\mathtt{r}}$, an infinite number of saddle periodic orbits, including $\Gamma^{\pm}$ (also known as the primary periodic orbits) [41, 24, 28, 21]. This bifurcation at $\mu = 0$ is also referred to as a homoclinic explosion point. It marks the beginning of the so-called preturbulent regime, where one finds a hyperbolic set that contains infinitely many saddle periodic orbits [28, 25]. As a result, there are orbits with arbitrarily long transients, but $p^{\pm}$ are still the only attractors [41, 16]. The preturbulent regime ends at $\rho_{\mathrm{E}} \approx 24.0579$, where there is a pair of heteroclinic connections between $\mathbf{0}$ and $\Gamma^{\pm}$; together with structurally stable connections from $\Gamma^{\pm}$ back to $\mathbf{0}$, it forms a pair of EtoP cycles. We call this heteroclinic bifurcation EtoP for equilibrium to periodic orbit. At EtoP the two branches of $W^u(\mathbf{0})$ no longer converge to $p^{\pm}$, respectively, but rather lie in the stable manifold $W^s(\Gamma^{\pm})$ of $\Gamma^{\pm}$. Past EtoP, the one-dimensional invariant manifold $W^u(\mathbf{0})$ never settles down to simple behaviour, creating

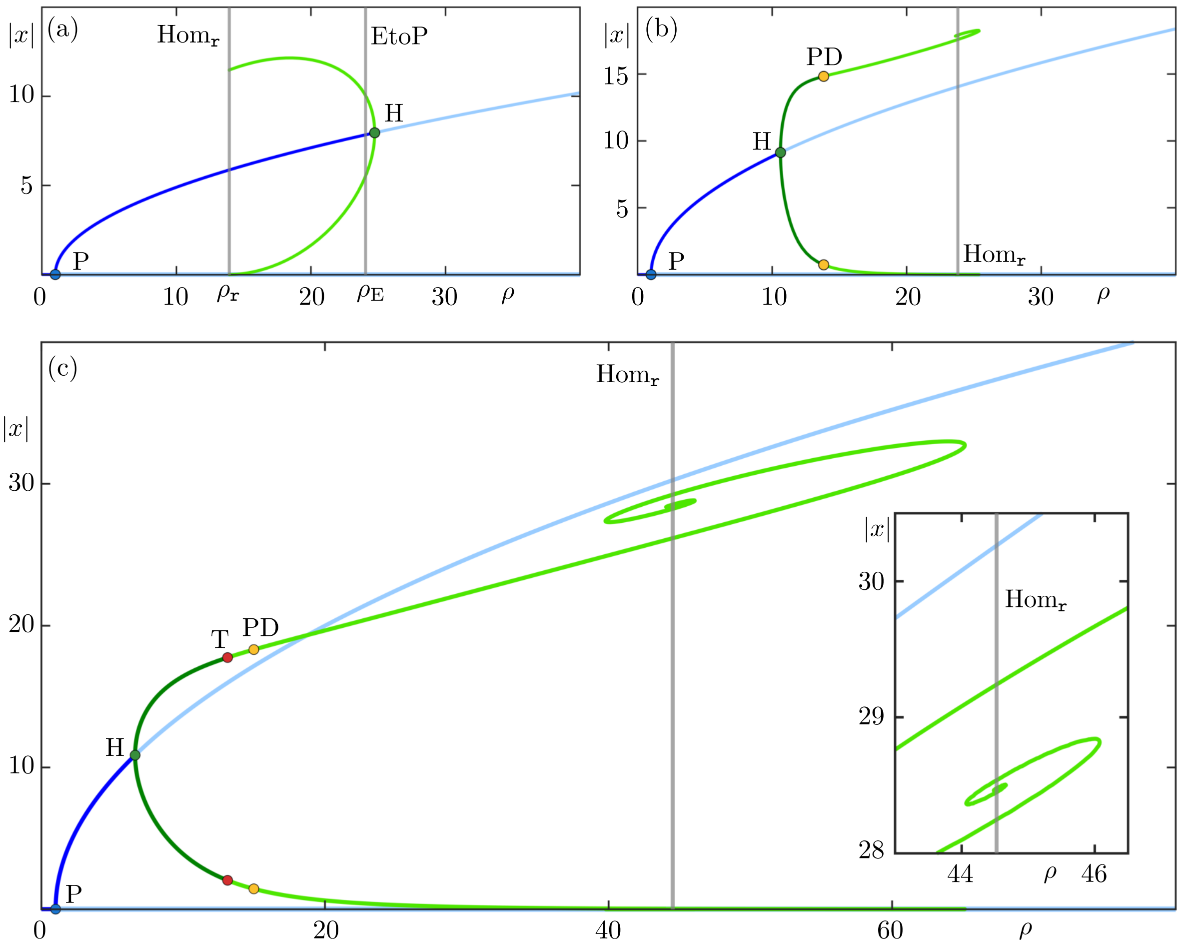

Figure 2: One-parameter bifurcation diagrams of (1) in ρ for $\mu = 0$ (a), $\mu = 4$ (b), and $\mu = 7$ (c), where branches are represented by $|x|$. Shown are branches of equilibria (dark blue when stable and light blue when saddles) and periodic orbits (dark green when stable and light green when saddles) represented by their minimum and maximum value of $|x|$. Also shown are points P of pitchfork, H of Hopf, PD of period-doubling and T of torus bifurcation, together with the vertical lines Hom$_{\mathtt{r}}$ of homoclinic and EtoP of equilibrium to periodic orbit bifurcation.

a chaotic attractor: the famous Lorenz attractor. It initially coexists with $p^{\pm}$ until they lose stability at H; subsequently, the Lorenz attractor is the sole attractor of system (1) with $\mu = 0$. It is pseudohyperbolic over a range of ρ-values up to about $\rho = 31.01$; see [12, 10] for details.

Figure 2(b) shows the case for $\mu = 4$. Initially, up to $\rho \approx 10$, the bifurcation structure is as for $\mu = 0$. However, the Hopf bifurcation H now occurs much earlier at $\rho \approx 10.6227$, before the homoclinic bifurcation Hom$_{\mathtt{r}}$ at $\rho \approx 23.8079$. This change in the order of H and Hom$_{\mathtt{r}}$ means, in particular, that the Hopf bifurcation is now supercritical: the bifurcating pair of periodic orbits exist to the right of H and $\Gamma^{\pm}$ are initially stable. These two periodic orbits are the only attractors of system (1) until they lose stability in a supercritical period-doubling bifurcation PD at $\rho \approx 14.2488$. Here, a pair of stable period-doubled periodic orbits is born (not shown); this process continues in a period-doubling cascade that creates a pair of chaotic attractors. Past PD, the periodic orbits $\Gamma^{\pm}$ are of saddle type with three-dimensional stable manifolds. As shown in panel (b), they disappear in the homoclinic bifurcation Hom$_{\mathtt{r}}$ at $\rho \approx 23.8079$, but in a spiralling manner: they loop around a point on Hom$_{\mathtt{r}}$ while converging to it. Additionally, note that system (1) with $\mu = 4$ does not have an EtoP bifurcation.

Finally, we show in Fig. 2(c) the case $\mu = 7$. In a broad sense, the bifurcation structure is as for $\mu = 4$. A difference is that, this time, the stable periodic orbits $\Gamma^{\pm}$ emanating from the Hopf bifurcation lose stability in a torus bifurcation T at $\rho \approx 13.067$. Past this point, $\Gamma^{\pm}$ are of saddle type with two-dimensional stable manifolds. At $\rho \approx 14.9813$, the periodic orbits $\Gamma^{\pm}$ undergo a subcritical period-doubling bifurcation PD and, subsequently, the dimension of their stable manifold is three. As for $\mu = 4$, the periodic orbits $\Gamma^{\pm}$ disappear at the homoclinic bifurcation $\mathrm{Hom}_{\mathtt{r}}$, which now occurs at the much larger value $\rho \approx 44.5255$; note the change in scale in panel (c) when compared to panels (a) and (b). The spiralling of the branches of $\Gamma^{\pm}$ in Fig. 2(c) is now much more pronounced; see the inset in panel (c). As for $\mu = 4$, there is no EtoP bifurcation for $\mu = 7$.

The fact that the branches of $\Gamma^{\pm}$ spiral into a point on $\mathrm{Hom}_{\mathtt{r}}$ indicates a Shilnikov-type homoclinic bifurcation. In Fig. 3, we illustrate in different projections the pair of Shilnikov homoclinic orbits to $\mathbf{0}$ at $\mathrm{Hom}_{\mathtt{r}}$ for $\mu = 4$ in row (a) and for $\mu = 7$ in row (b). They are formed by the two branches of $W^u(\mathbf{0})$, which we denote $W^u_+(\mathbf{0})$ and $W^u_-(\mathbf{0})$. Also shown in Fig. 3 is the symmetric pair of equilibria $p^{\pm}$. Figure 3(a1) is the projection onto (x, z, w)-space, which illustrates the two Shilnikov homoclinic orbits approaching $\mathbf{0}$ in a spiralling manner. This behaviour is also clearly observed in the projection onto the (z, w)-plane in panel (a2); note that the pair of homoclinic orbits coincide in this projection. The projection onto the (x, y)-plane in panel (a3) shows how $W^u_+(\mathbf{0})$ and $W^u_-(\mathbf{0})$ loop around p^+ and p^-, respectively, before converging to $\mathbf{0}$; in this projection the spiralling behaviour around $\mathbf{0}$ is not visible. Figure 3 shows similar projections onto (x, z, w)-space in panel (b1) and onto the (z, w)-plane in panel (b2), which illustrates that the pair of Shilnikov homoclinic orbits for $\mu = 7$, exhibits more pronounced spiralling around $\mathbf{0}$. The projection onto the (x, y)-plane in panel (b3) is similar to that in panel (a3), but the pair of equilibria $p^{\pm}$ is now beyond the loops (and outside the shown range).

To get a sense of the transition between panels (a) to (c) in Fig. 2, we now consider the associated two-parameter bifurcation diagram of system (1) in the (ρ, μ)-plane. Figure 4 shows the curves $\rho = 1$ of pitchfork bifurcation P, and

$$\mu = \frac{8}{3}\sqrt{\left(\frac{53110 + 21823\rho - 969\rho^2}{925 + 2860\rho - 969\rho^2}\right)}, \qquad \frac{185}{57} < \rho < \frac{470}{19}, \tag{2}$$

of Hopf bifurcation H. Hence, P is a vertical line, and H has the vertical asymptote $\rho = 185/57$. The other codimension-one bifurcation curves need to be computed numerically, which we achieve with the package `AUTO` [13, 14] by starting from the corresponding bifurcation points in Fig. 2. In particular, the continuation of $\mathrm{Hom}_{\mathtt{r}}$ from the point $(\rho_{\mathtt{r}}, 0)$ gives the corresponding curve in Fig. 4, which is monotonically increasing with $\rho > \rho_{\mathtt{r}}$. Similarly, we continue and show in Fig. 4 the curve EtoP starting from the point $(\rho_{\mathrm{E}}, 0)$; it exists for decreasing ρ, has a maximum at $\mu \approx 1.4161$, and ends at the point $(\rho_{\mathtt{r}}, 0)$. Notice that the curves EtoP and $\mathrm{Hom}_{\mathtt{r}}$ approach each other very closely as they converge to the point $(\rho_{\mathtt{r}}, 0)$. By continuation from the point PD for $\mu = 4$, we find the curve PD of period-doubling bifurcation; it grows when continued in the direction of increasing μ and leaves the shown range of Fig. 4. In the direction of decreasing μ, the curve PD also ends at the point $(\rho_{\mathtt{r}}, 0)$. From Fig. 2, we know that there must be a change in criticality on the curve PD in the range $4 < \mu < 7$. The point $(\rho, \mu) \approx (14.2021, 5.2156)$ at which this happens is detected by `AUTO` as the codimension-two 1:2 resonance point R_2. Bifurcation theory suggests the existence of a torus bifurcation near R_2 [31]. In fact, we find that the curve T of torus bifurcation, when continued from the point T in Fig. 2(c), indeed, ends on the curve PD at R_2; when continued for increasing μ, the curve T grows beyond bound and leaves the frame of Fig. 4. We also know from Fig. 2 that there must be a criticality change on the curve H in the range $0 < \mu < 4$. We find it by continuing the curve H numerically with `AUTO` instead of using the analytical expression (2); in this way, we detect the codimension-two generalized Hopf point GH at $(\rho, \mu) \approx (13.2731, 3.0465)$ where the

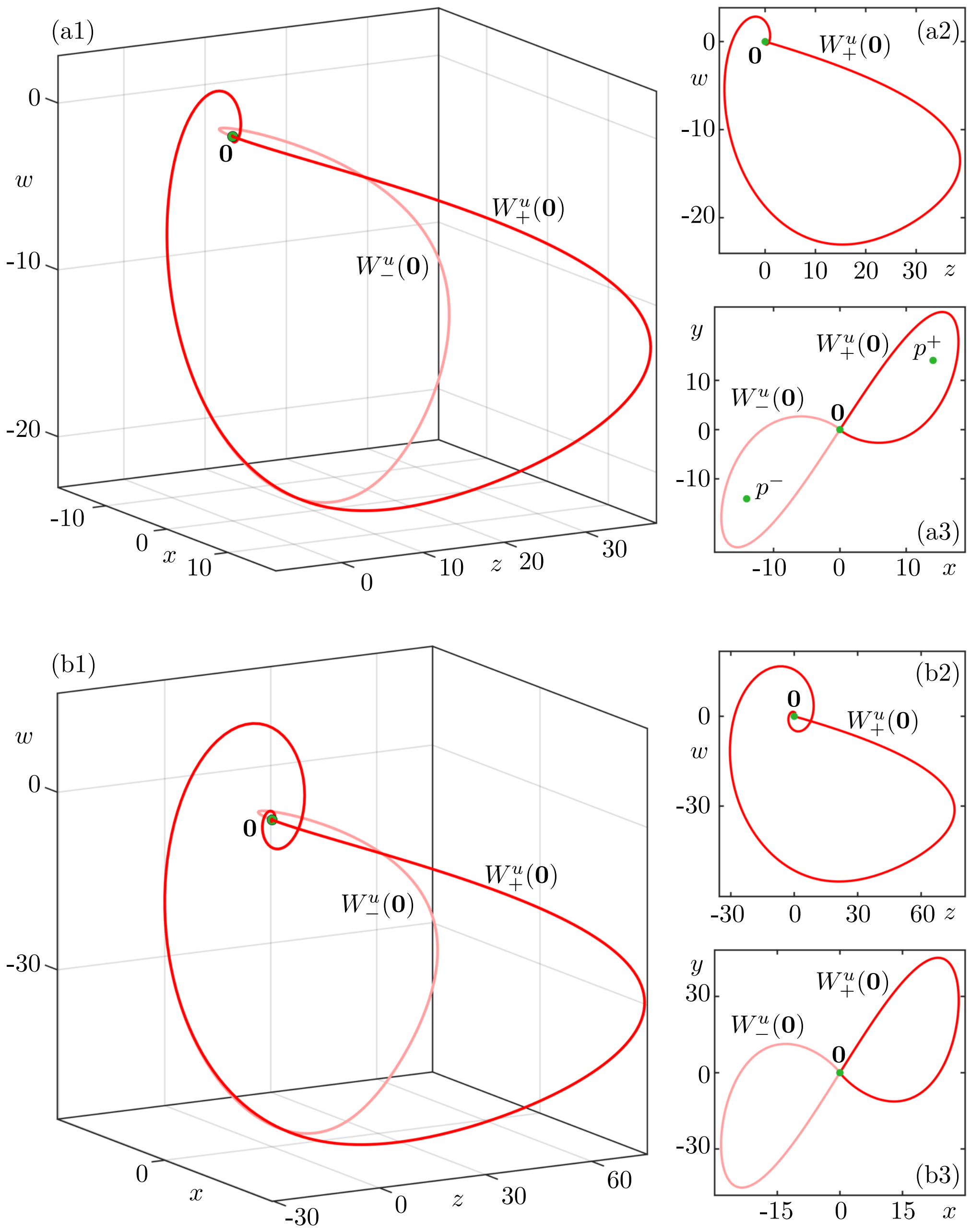

Figure 3: The homoclinic orbit $\mathrm{Hom}_{\mathtt{r}}$ of (1) with $\mathbf{0}$ and $p^{\pm}$ (green dots) for $\mu = 4$ and $\rho \approx 23.8078$ (a) and for $\mu = 7$ and $\rho \approx 44.5255$ (b), formed by $W^u_+(\mathbf{0})$ (red curve); also shown is the symmetric counterpart formed by $W^u_-(\mathbf{0})$ (light-red curve). Shown are projections onto (x, z, w)-space (a1), (b1), onto the (z, w)-plane (a2), (b2), and onto the (x, y)-plane (a3), (b3).

criticality of H changes. The unfolding of GH gives rise to a curve F of fold (or saddle-node) bifurcation of periodic orbits [31], which we followed and show in Fig. 4. Note that the curve F connects GH with the point $(\rho_{\mathtt{r}}, 0)$ and was, thus, not observed in Fig. 2.

Overall, Fig. 4 explains what we have seen in the three one-parameter bifurcation diagrams of Fig. 2. In particular, the homoclinic explosion point of the Lorenz system at $(\rho_{\mathtt{r}}, 0)$ emerges as an organizing centre of the two-parameter bifurcation diagram in the (ρ, μ)-plane. Not only is it the endpoint of the curve $\mathrm{Hom}_{\mathtt{r}}$, but it also gives rise to the curves EtoP, PD and F that are not part of the bifurcation sequence near $\rho_{\mathtt{r}}$ when $\mu = 0$.

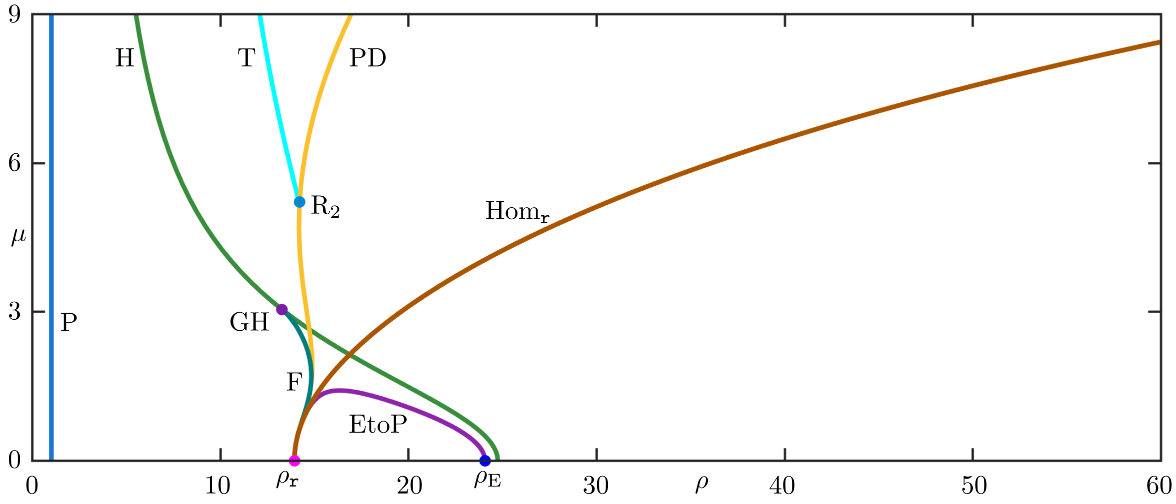

Figure 4: Two-parameter bifurcation diagram of (1) in the (ρ, μ)-plane with curves P (blue) of pitchfork, H (green) of Hopf, T (cyan) of torus, PD (yellow) of period-doubling, F (teal) of fold of periodic orbits, EtoP (purple) of equilibrium to periodic orbit, and $\mathrm{Hom}_{\mathtt{r}}$ (brown) of homoclinic bifurcation. Also shown are the codimension-two points GH (purple) of generalized Hopf and R_2 (light blue) of 1:2 resonance bifurcation.

A global ingredient in the two-parameter bifurcation diagram of Fig. 4 is the curve EtoP. We conclude this section by examining the associated connecting orbit at its two points with $\mu = 1.2$. The top row of Fig. 5 shows the EtoP connection, where $W^u_+(\mathbf{0})$ connects to Γ^- in the (x, y, z)-space, along with the equilibria $\mathbf{0}$ and $p^{\pm}$, and the bottom row are projections onto the (x, y)-plane. For points near $(\rho_E, 0)$, the EtoP connection resembles that of the classic Lorenz equations (see [15, Fig. 2]), as depicted in panels (a1) and (a2) of Fig. 5 for $\rho \approx 19.015$. As ρ decreases, the periodic orbit Γ^- grows, as shown in panels (b1) to (b3) for $\rho \approx 14.954$, where both the EtoP connection and Γ^- approach the limiting pair of homoclinic orbits. This is particularly evident in the projection onto the (x, y)-plane in panel (b2). The enlargement near $\mathbf{0}$ in panel (b3) reveals that this is, indeed, still an EtoP connection. Note that there is no spiralling near $\mathbf{0}$ in any panels of Fig. 5 because this only occurs in the stable subspace near $\mathbf{0}$, which is not involved in the EtoP connection.

3 Homoclinic bifurcations of different symbol sequences

In previous research into the classic Lorenz system, the authors of [15] systematically followed $2^9 = 512$ heteroclinic orbits connecting p^+ to $\mathbf{0}$ in the parameter ρ; each of them was found to end at a particular pair of homoclinic orbits to $\mathbf{0}$ at a well-defined value of $\rho > \rho_{\mathtt{r}}$. In this way, 116 different homoclinic orbits were found, which were all identified as homoclinic explosion points that give rise to infinitely many periodic orbits; see [41] and, in particular, [15] for more details and available data of these so-called admissible homoclinic orbits. The homoclinic orbits found in [15] make longer and more complicated 'excursions around' p^+ and p^- compared to the homoclinic orbit $\mathrm{Hom}_{\mathtt{r}}$. They are described with a finite symbol sequence based on $W^u_+(\mathbf{0})$, defined in [15] as

$$\mathtt{r}h_1 \cdots h_k \quad \text{where} \left\{ \begin{array}{lcll} h_j & = & \mathtt{l} & \text{if the } j\text{th excursion is around } p^-, \\ h_j & = & \mathtt{r} & \text{if the } j\text{th excursion is around } p^+, \end{array} \right. \tag{3}$$

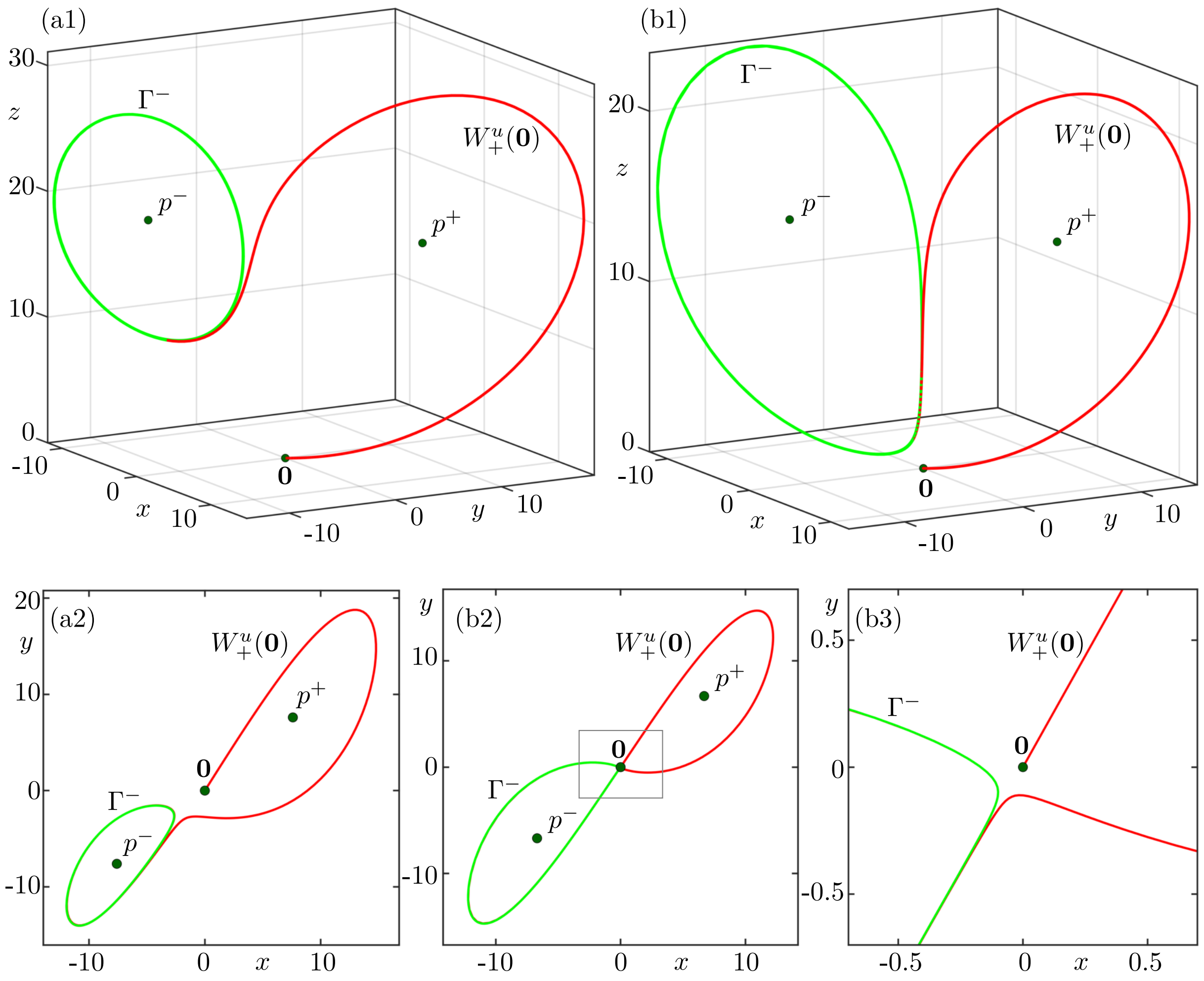

Figure 5: The EtoP connection of system (1) for $\rho \approx 19.015$, $\mu = 1.2$ in panels (a1), (a2), and for $\rho \approx 14.954$, $\mu = 1.2$ in panels (b1)–(b3). Shown are projections onto (x, y, z)-space (top row) and onto the (x, y)-plane (bottom row). Panel (b3) is an enlargement of the grey rectangle in panel (b2).

for some $k \in \mathbb{N}$, which we call the *level* of the symbol sequence; the symbol sequence $\mathtt{r}$ of the basic homoclinic orbit $\mathrm{Hom}_{\mathtt{r}}$ has level zero and the 116 homoclinic orbits found in [15] have symbol sequences up to level nine. The first symbol in (3) does not give any extra information: it is always $\mathtt{r}$ because we are considering the symbol sequences of the positive branch $W^u_+(\mathbf{0})$, which has its first excursion around p^+; see figures 3, 7 and 8. Its symmetric counterpart is the symbol sequence of $W^u_-(\mathbf{0})$ given by $\overline{\mathtt{r}h_1 \cdots h_k} = \mathtt{l}\bar{h}_1 \cdots \bar{h}_k$, where $\bar{\mathtt{r}} = \mathtt{l}$ and $\bar{\mathtt{l}} = \mathtt{r}$. The symbol sequence can be computed efficiently by considering maxima and minima of the time series of x of $W^u_+(\mathbf{0})$; see Se. 4, where we define the symbol sequence of $W^u_+(\mathbf{0})$ more generally.

In the classic Lorenz equations, that is, for $\mu = 0$ in system (1), past the homoclinic bifurcation $\mathrm{Hom}_{\mathtt{r}}$, the branch $W^u_+(\mathbf{0})$ immediately switches, after its first excursion around p^+, to the region with negative x. Therefore, $W^u_+(\mathbf{0})$ makes at least one excursion around p^- before returning to $\mathbf{0}$, and $h_1 = \mathtt{l}$ for all symbol sequences with $k \geq 1$ [15, 41]. We continue the 21 homoclinic orbits from [15] with symbol sequences up to level six as curves in the (ρ, μ)-plane. We refer to them as secondary homoclinic orbits Hom_s, with a given symbol sequence s. Figure 6 shows the bifurcation curves from Fig. 4 together with these 21 curves of secondary homoclinic orbits Hom_s; their symbol sequences are shown at the bottom of the figure. Panel (a) of Fig. 6

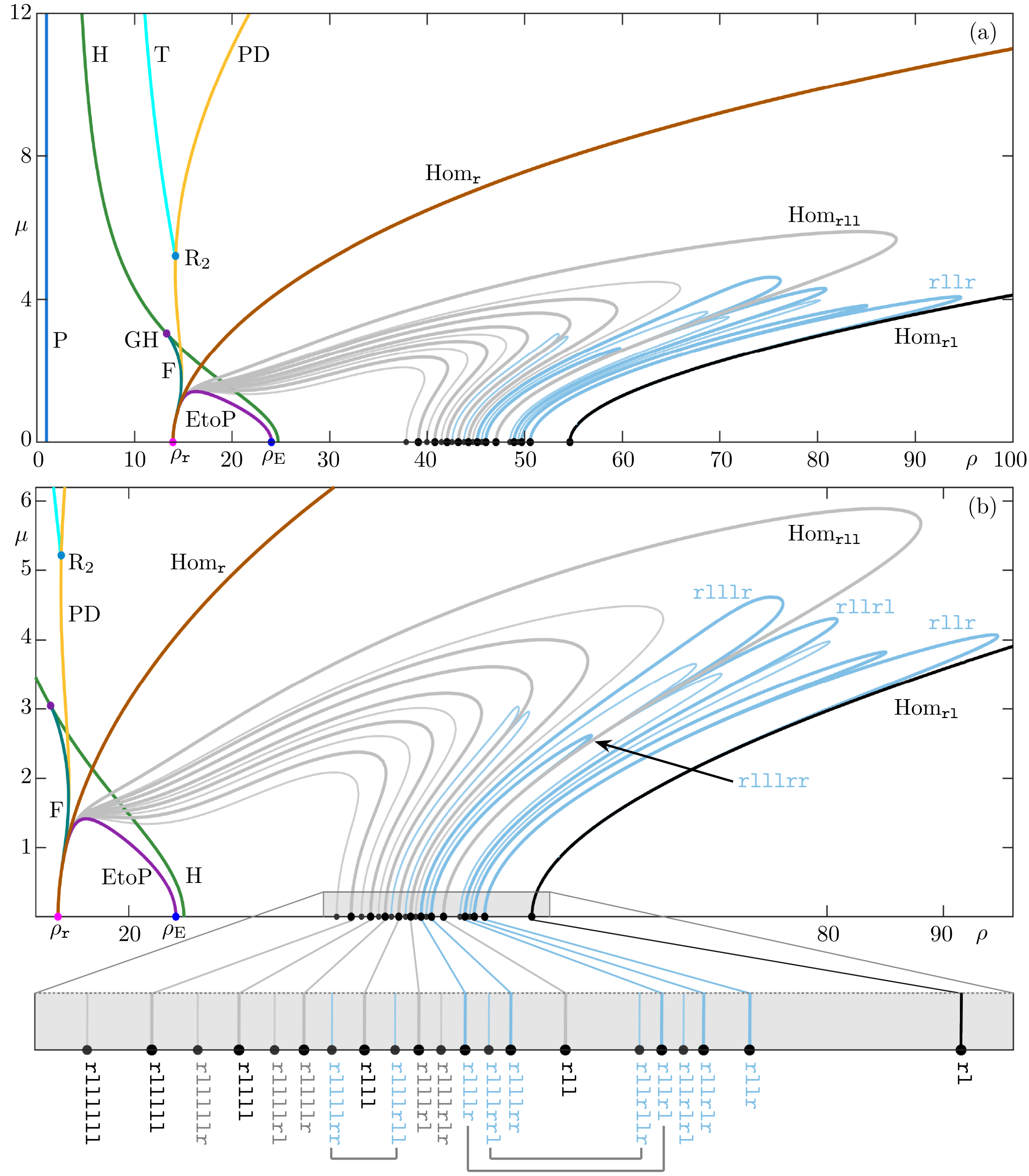

Figure 6: Two-parameter bifurcation diagram from Fig. 4 with the 21 curves of secondary homoclinic bifurcation Hom_s up to level six, with those of level six plotted as thinner curves; their finite symbol sequences s are shown at the bottom and summarized in Table 1 and Table 2. We distinguish curves that end at the point $(\rho_{\mathtt{r}}, 0)$ (group I, grey), those that end at a different homoclinic bifurcation point (group II, light blue), and the curve $\mathrm{Hom}_{\mathtt{rl}}$ (black). Panel (a) shows a larger part of the (ρ, μ)-plane and panel (b) is an enlargement; under-brackets indicate twin homoclinic orbits.

shows a larger part of the (ρ, μ)-plane, and panel (b) is an enlargement that focuses on the 21 curves Hom_s; here, the curves with $k \leq 5$ are shown thicker. We computed these curves Hom_s

symbol	ρ-value from [15]	limit symbol	ρ at endpoint
`rl`	54.645952		∞
`rll`	47.053443	`r`	13.9565
`rlllrlr`	44.668849	`r`	13.9565
`rlllrl`	44.240808	`r`	13.9565
`rlll`	43.198042	`r`	13.9565
`rllllr`	42.034581	`r`	13.9565
`rllllrl`	41.472638	`r`	13.9565
`rllll`	40.788829	`r`	13.9565
`rllllllr`	39.996627	`r`	13.9565
`rlllll`	39.115749	`r`	13.9565
`rllllll`	37.875935	`r`	13.9565
`rL`	24.0579	`r`	13.9565

Table 1: Homoclinic orbits Hom_s in group I of given finite symbol sequence s up to level six, with the respective values of ρ at the begin and endpoints on the ρ-axis of their corresponding bifurcation curves in the (ρ, μ)-plane. The subfamily $\mathtt{rl}^k$ is highlighted in green. All these homoclinic orbits limit onto $\mathrm{Hom}_\mathtt{r}$; compare with Fig. 6 and Fig. 7.

with `AUTO` by starting from the available data in [15]. For the respective ρ-value with $\mu = 0$, we generate four-dimensional starting data and then continue the respective curves of homoclinic orbits in the (ρ, μ)-plane as the solution family of a suitable boundary value problem; see [30] for details. As with the primary homoclinic bifurcation $\mathrm{Hom}_\mathtt{r}$, all homoclinic bifurcations of different finite symbol sequences are of Shilnikov type when $\mu > 0$.

Figure 6 shows that the curves of secondary homoclinic orbits Hom_s divide into groups that behave differently. The curve $\mathrm{Hom}_\mathtt{rl}$ is the only homoclinic bifurcation of level 1, and it leaves the shown parameter region in a manner similar to $\mathrm{Hom}_\mathtt{r}$. We find that the curve $\mathrm{Hom}_\mathtt{rl}$ also goes off to infinity. The curve $\mathrm{Hom}_\mathtt{r}$ is the homoclinic bifurcation curve with the smallest ρ-value with $\mu = 0$, and $\mathrm{Hom}_\mathtt{rl}$ has the largest value of ρ [15]. All other curves of secondary homoclinic bifurcation lie in the region bounded by $\mathrm{Hom}_\mathtt{r}$ and $\mathrm{Hom}_\mathtt{rl}$. Amazingly, none of these curves leave the shown parameter region. Rather, they come in two groups: curves that end at the (first) homoclinic explosion point $(\rho_\mathtt{r}, 0)$ of the Lorenz system, which we will refer to as group I, and curves that end at another homoclinic explosion point of the Lorenz system (with $\mu = 0$), which we call group II. These two groups are distinguished by colour in Fig. 6; moreover, their properties are summarized in Table 1 and Table 2, respectively, in terms of the ρ-values at their begin and endpoints and the associated symbol sequences.

We first consider and describe the curves in group I. Figure 7 shows some examples of secondary homoclinic orbits Hom_s in this group in projection onto the (x, y)-plane, namely, those for fixed $\mu = 1.2$ with corresponding values of ρ, and with symbol sequences as shown in each panel of the figure. In particular, the subfamily of homoclinic orbits Hom_s with $s = \mathtt{rl}^k$ is from group I, and its symbol sequence is highlighted in bold in Fig. 6 and in green in Table 1. Panels (a1)–(a6) of Fig. 7 show the corresponding homoclinic orbits up to level $k = 6$. The importance of this subfamily is that it has the EtoP cycle as its limit; that is, as $k \to \infty$, we have that $\mathtt{rl}^k \to \mathtt{rL}$, where the symbol `L` represents infinitely many loops around Γ^- and, hence, excursions around p^-. This convergence was identified in [15] for the corresponding homoclinic bifurcation points of the Lorenz system on the ρ-axis, which converge to the point $(\rho_\mathrm{E}, 0)$. We observe, and conjecture here, that the subfamily of curves Hom_s with $s = \mathtt{rl}^k$ also converges to the curve EtoP in the two-parameter (ρ, μ)-plane of system (1) as $k \to \infty$. However, this convergence is slow and so only hinted at in Fig. 6, as well as Fig. 7(a1)–(a6).

In addition to this subfamily, we find other secondary homoclinic bifurcations Hom_s in group

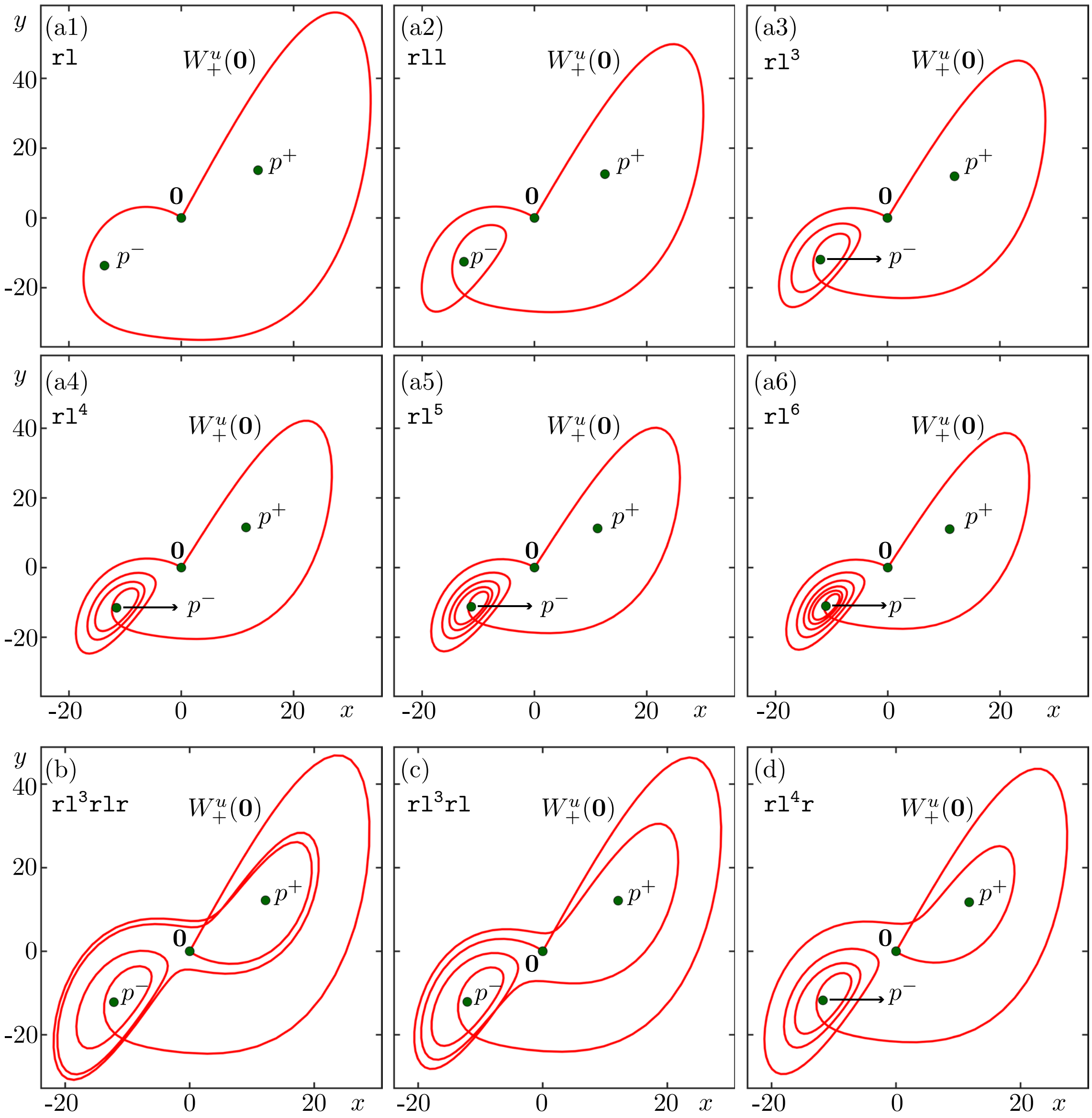

Figure 7: Homoclinic orbits Hom_s for $\mu = 1.2$ from group I as listed in Table 1, formed by $W^u_+(\mathbf{0})$ and shown with $\mathbf{0}$ and $p^\pm$ (green dots) in projection onto the (x, y)-plane. Here $\rho \approx 59.2656$ (a1), $\rho \approx 50.1550$ (a2), $\rho \approx 45.4384$ (a3), $\rho \approx 42.4947$ (a4), $\rho \approx 40.4656$ (a5), $\rho \approx 38.9735$ (a6), $\rho \approx 47.2593$ (b), $\rho \approx 46.7092$ (c), and $\rho \approx 44.0306$ (d). Their symbol sequences s are indicated in each panel.

I, and panels (b)–(d) of Fig. 7 show three examples. We were unable to tease out which symbol sequences correspond to homoclinic orbits from group I, but we believe there to be infinitely many that are organized in other subfamilies. Observe in the enlargement panel (b) of Fig. 6 that any other subfamilies in group I lie nested in between curves of the subfamily $\mathrm{Hom}_{\mathtt{rl}^k}$; this is necessarily the case because curves of homoclinic orbits to $\mathbf{0}$ cannot intersect. Therefore, we conjecture that any subfamily in group I converges similarly to the curve EtoP as the level of the symbol sequence goes to infinity.

We now consider the curves of secondary homoclinic orbits Hom_s in group II; their properties are summarized in Table 2. Observe that the secondary homoclinic orbits in group II have different endpoints with associated symbol sequences. Figures 8 and 9 illustrate some of the secondary homoclinic orbits in group II in projection onto the (x, y)-plane and as a time series of

symbol	ρ-value from [15]	limit symbol	ρ at endpoint
`rllr`	50.590467	`rl`	54.645952
`rllrl`	48.900976	`rll`	47.053443
`rlllr`	45.128887	`rll`	47.053443
`rllrlr`	49.703500	`rllr`	50.590467
`rlllrr`	46.005196	`rll`	47.053443
`rllrlrl`	49.320171	`rllrl`	48.900976
`rllrllr`	48.476611	`rll`	47.053443
`rlllrrl`	45.585034	`rll`	47.053443
`rlllrll`	43.786551	`rlll`	43.198042
`rllllrr`	42.573041	`rlll`	43.198042

Table 2: Homoclinic orbits Hom_s in group II of given finite symbol sequence s up to level six, with the respective values of ρ at the begin and endpoints on the ρ-axis of their corresponding bifurcation curves in the (ρ, μ)-plane. These homoclinic orbits limit on different ones as given by the limit symbols; compare with Fig. 6, Fig. 8 and Fig. 9.

x. In both figures, the first column shows homoclinic orbits with $\mu = 1.2$ for symbol sequences as shown in each panel; the second column shows each homoclinic orbit when continued practically to its limit, the endpoint with $\mu \approx 0$; here, the first segment of the orbit that gives the shown limiting symbol sequence is shown darker than the 'tail'. The third column presents the time series of x for respective homoclinic orbits over the normalized time interval $[0, 1]$.

Figure 8 illustrates a particular subfamily in group II. Panel (a1) shows the secondary homoclinic orbit with symbol sequence $s = \texttt{rllr}$ near the start of the continuation at $\mu = 1.2$ when $\rho \approx 54.5225$. When continued in the (ρ, μ)-plane, the curve converges to the endpoint $(\rho, \mu) \approx (54.645952, 0)$, which corresponds to the homoclinic orbit $\mathrm{Hom}_{\texttt{rl}}$, as is also suggested in Fig. 6. Observe in Fig. 8(a2) that $W^u_+(\mathbf{0})$ now comes very close to $\mathbf{0}$ well before it converges to $\mathbf{0}$. This is illustrated by the time series of x in panels (a3) and (a4): in panel (a4), the branch $W^u_+(\mathbf{0})$ spends a large amount of time near $\mathbf{0}$ after only the two loops `rl`. In the limit, the remaining segment of the homoclinic orbit with $s = \texttt{rllr}$ is no longer part of the connecting orbit because it is no longer reachable by $W^u_+(\mathbf{0})$. This is why we say that the secondary homoclinic orbit with symbol sequence $s = \texttt{rllr}$ converges to the homoclinic orbit $\mathrm{Hom}_{\texttt{rl}}$, 'dropping the tail' `lr`. This convergence behaviour is also observed in [15] for the classic Lorenz system when studying how (structurally stable) heteroclinic orbits connecting p^+ and $\mathbf{0}$ end at particular pairs of homoclinic orbits to $\mathbf{0}$ at well-defined values of $\rho > \rho_{\texttt{r}}$ when continued in the parameter ρ; in [15], however, the limit comprises the 'tail' of these heteroclinic orbits.

Note that, in Fig. 8(a2), the 'tail' is the symmetric counterpart of the limiting homoclinic orbit. That is, the homoclinic orbit with symbol sequence $s = \texttt{rllr} = \texttt{rl}\overline{\texttt{rl}}$, has `rl` as its limit. In Fig. 8(b1), we show a second example of this type of homoclinic orbit from group II, namely, Hom_s with $s = \texttt{rlllrr} = \texttt{rll}\overline{\texttt{rll}}$. Again, when continued in the (ρ, μ)-plane, as the endpoint $(\rho, \mu) \approx (47.0534, 0)$ of the curve Hom_s is approached, $W^u_+(\mathbf{0})$ comes very close to $\mathbf{0}$ before completing the last three oscillations. Indeed, panel (b2) shows how the homoclinic orbit with symbol sequence `rll` splits off in the limit; see also panels (b3) and (b4).

These two examples suggest that there is a subfamily in group II, for which Hom_s splits in the middle, with the second half of the symbol sequence being the symmetric counterpart of the first half. It is a natural conjecture that, for any finite (occurring) symbol sequence m, the homoclinic orbit with symbol sequence $m\overline{m}$ is in group II and has Hom_m as its limit. The data shown in Fig. 6 and Table 2 provides the only two examples illustrated in Fig. 8(a) and (b) from the family of homoclinic orbits up to level six. To support this conjecture, we also compute a homoclinic orbit of level seven, namely, Hom_s with $s = \texttt{rllrlrrl} = \texttt{rllr}\overline{\texttt{rllr}}$, which is part of

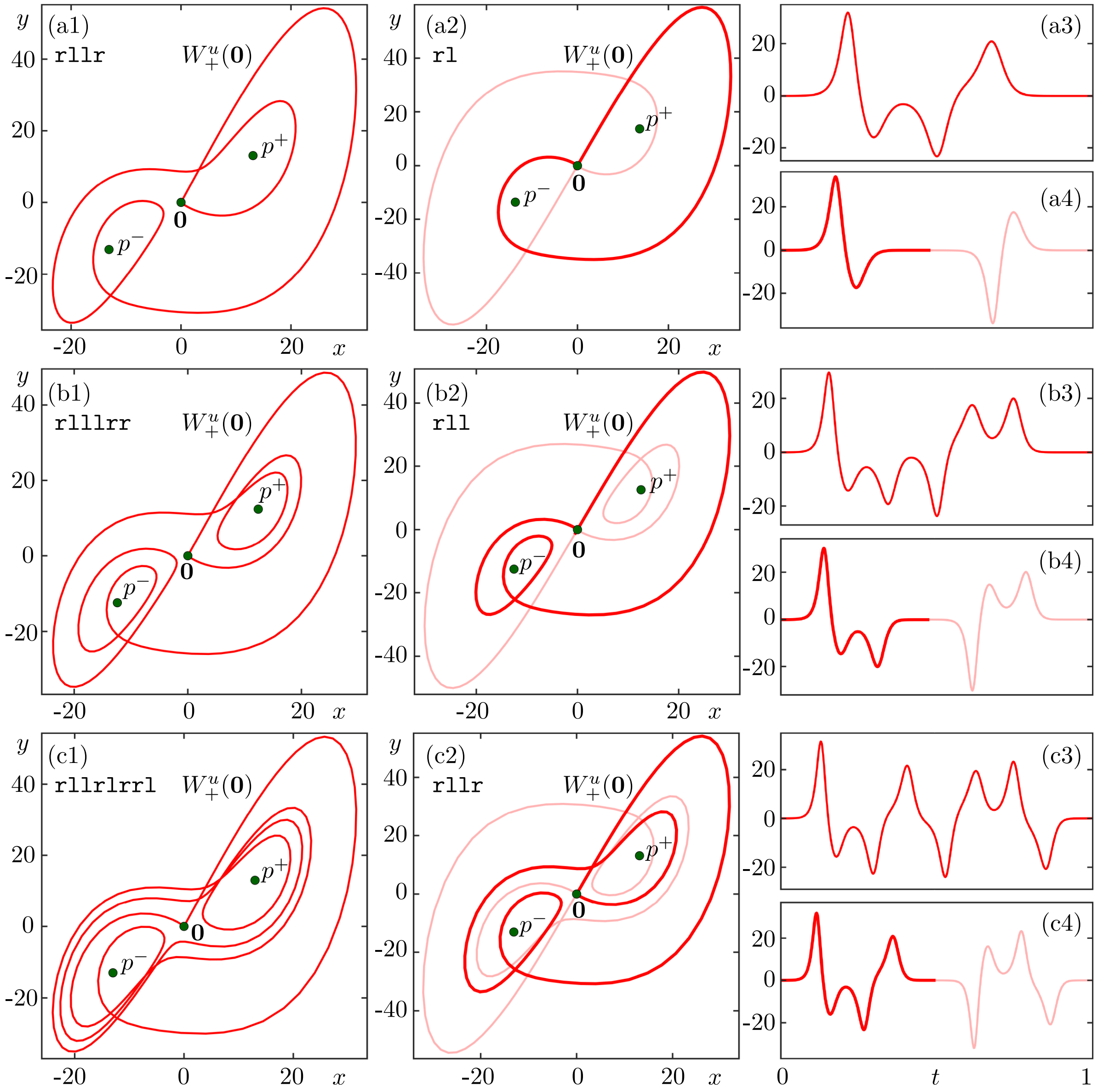

Figure 8: Homoclinic orbits Hom_s from group II from Table 2 shown with $\mathbf{0}$ and $p^{\pm}$ (green dots) in projection onto the (x, y)-plane and as time series of x. The respective homoclinic orbit is shown in the first column at $\mu = 1.2$, and in the second column near the endpoint of Hom_s with $\mu \approx 0$, where the limiting homoclinic orbit is dark red; the third column shows the two corresponding time series of x. Here $\rho \approx 54.5225$ (a1, a3), $\rho \approx 54.65$ (a2, a4), $\rho \approx 48.9370$ (b1, b3), $\rho \approx 47.05$ (b2, b4), $\rho \approx 53.6854$ (c1, c3), and $\rho \approx 50.59$ (c2, c4). The symbol sequences of Hom_s and the limiting homoclinic orbits are indicated in the first and second columns, respectively.

the available data in [15]. The continuation of this homoclinic orbit is shown in Fig. 8(c) in the same way. The homoclinic orbit is now more complicated but again splits in the middle and has Hom_m with $m = \texttt{rllr}$ as its limit, in agreement with the conjecture.

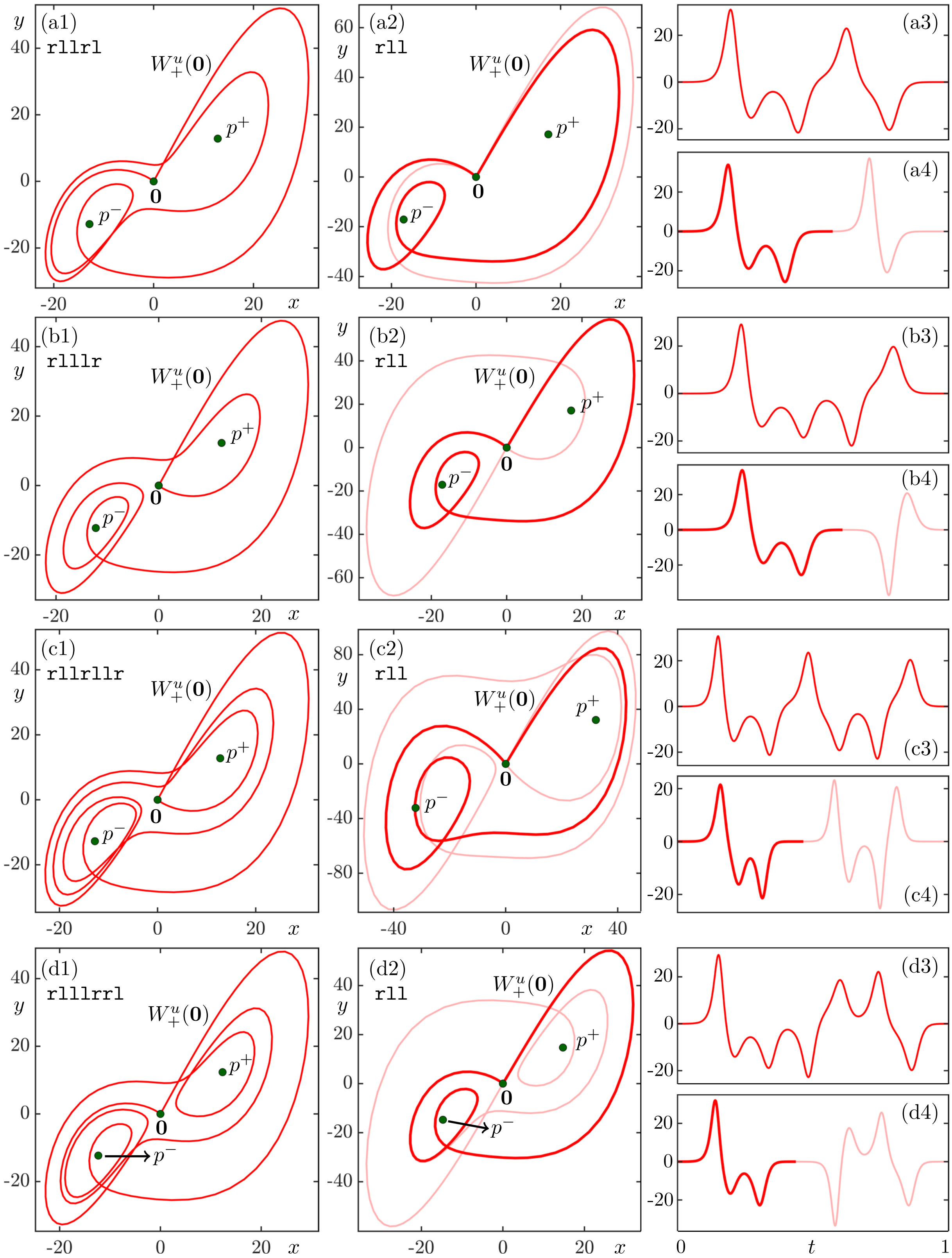

Figure 9: Twin homoclinic orbits Hom_{s_i} from group II with symbol sequences as indicated, shown with $\mathbf{0}$ and $p^{\pm}$ (green dots) as in Fig. 8. Here, $\rho \approx 52.39$ (a1, a3), $\rho \approx 47.83$ (b1, b3), $\rho \approx 51.86$ (c1, c3), $\rho \approx 48.40$ (d1, d3), and all homoclinic orbits converge to $\mathrm{Hom}_{\texttt{rll}}$ on the ρ-axis with $\rho \approx 47.05$ (a2, a4, b2, b4, c2, c4, d2, d4).

We observe in Fig. 6 that curves in group I appear to be accumulated, on either side, by pairs of curves in group II. The exceptions are $\mathrm{Hom}_{\mathtt{r}}$ and $\mathrm{Hom}_{\mathtt{rl}}$, which are only accumulated from the right and the left, respectively, because they form the boundary of all other secondary homoclinic curves. As a specific example, observe in the enlargement panel (b) of Fig. 6 the curves Hom_{s_1} and Hom_{s_2} with symbol sequences $s_1 = \mathtt{rllrl}$ and $s_2 = \mathtt{rlllr}$ that approach Hom_s with $s = \mathtt{rll}$ from the right and the left, respectively. We illustrate the associated convergence of these homoclinic orbits in Fig. 9(a) and (b). Panels (a1) and (b1) show the curves Hom_{s_1} and Hom_{s_2} near the start of the continuation at $\mu = 1.2$, when $\rho \approx 52.39$ and $\rho \approx 47.83$, respectively. When they are continued in the (ρ, μ)-plane, the homoclinic orbit $\mathrm{Hom}_{\mathtt{rll}}$ splits off as the endpoint $(\rho, \mu) \approx (47.0534,\ 0)$ of the curves is approached. This is highlighted in panels (a2) and (b2) by a darker colour and is illustrated further in panels (a3), (a4) and (b3), (b4) in terms of the time series of x over the normalized time interval $[0, 1]$. Note that we can write $s_2 = \mathtt{rlllr} = \mathtt{rll}\overline{\mathtt{rl}}$, which we call the 'twin' of $s_1 = \mathtt{rllrl}$; such twin homoclinic orbits are indicated by brackets in Fig. 6(b) and Table 2.

We show a second example in Fig. 9 (c) and (d) of this type of twin homoclinic orbits in group II, namely, the pair with $s_1 = \mathtt{rllrllr}$ and $s_2 = \mathtt{rlllrrl} = \mathtt{rll}\overline{\mathtt{rllr}}$ that also approach $\mathrm{Hom}_{\mathtt{rll}}$ from the right and left, respectively. Again, as the endpoint $(\rho, \mu) \approx (47.0534,\ 0)$ of the curves Hom_{s_1} and Hom_{s_2} is approached during the continuation, the segment with symbol sequence $\mathtt{rll}$ splits off, as highlighted in panels (c2) and (d2); see also panels (c3), (c4) and (d3), (d4) where we show the respective two instances of the pair of homoclinic orbits in terms of the time series of x. From the data we have, we observe and conjecture that the twin homoclinic orbits Hom_{s_i} with $s_1 = mv$ and $s_2 = m\overline{v}$ for (occurring) finite symbol sequences m and v are in group II, and have the homoclinic orbit Hom_m as their limit. Indeed, there is another example in Fig. 6 and Table 2 that agrees with the conjecture, namely, the twin pair Hom_{s_i} with $s_1 = \mathtt{rllllrr}$ and $s_2 = \mathtt{rlllrll} = \mathtt{rlll}\overline{\mathtt{lrr}}$ that converges to Hom_s with $s = \mathtt{rlll}$.

From the 116 admissible homoclinic orbits up to level six found in [15], we find that two give rise to curves in the (ρ, μ)-plane with endpoints at a limiting homoclinic orbit from group II. These two homoclinic orbits are Hom_{s_i} with $s_1 = \mathtt{rllrlr}$ and $s_2 = \mathtt{rllrlrl}$, which converge to $\mathtt{rllr}$ and $\mathtt{rllrl}$, respectively. It is unclear from the available data for which other symbol sequences one finds convergence to group II, but there will also be infinitely many of them.

Note in the enlargement panel (b) of Fig. 6 that the curve Hom_{s_1} with $s_1 = \mathtt{rlllrr}$, shown in Fig. 8(b), converges to Hom_m with $m = \mathtt{rll}$, but its twin Hom_{s_2} with $s_2 = \mathtt{rllrll}$ is not in Fig. 6 nor Table 2. Indeed, s_2 repeats the sequence $\mathtt{rll}$ and, as such, was not obtained in [15] (via the continuation of heteroclinic orbits) as an 'admissible' homoclinic explosion point [41]. Hence, at this point it is unclear whether Hom_{s_2} with $\mathtt{rllrll}$ actually exists in system (1), for $\mu > 0$.

A final note regarding Fig. 6 is that all the curves of secondary homoclinic bifurcation Hom_s are bounded by the main homoclinic bifurcation $\mathrm{Hom}_{\mathtt{r}}$. In particular, they are well away from $(\rho^*, \mu^*) = (25, 7)$, cited in [23] as the parameter point where a wild pseudohyperbolic chaotic attractor exists. While our results in this section reveal properties of the homoclinic explosion point $(\rho, \mu) = (\rho_{\mathtt{r}}, 0)$ and how it organizes the dynamics of system (1) that are directly associated with the Lorenz system, they do not explain (by themselves) the emergence of a wild pseudohyperbolic chaotic attractor.

4 Kneading Diagram of the unstable manifold of the origin

In an effort to find other global bifurcations, homoclinic or otherwise, we employ a parameter sweeping technique that determines regions in the (ρ, μ)-plane with different values of a topological invariant. This is an established way of detecting regions in a parameter plane with different qualitative behaviour; see [19, 8, 6, 5, 48] for different examples of this approach. Specifically, we consider the so-called kneading diagram that encodes the 'fate' of $W^u_+(\mathbf{0})$ for any parameter point in the (ρ, μ)-plane because this branch of the unstable manifold of $\mathbf{0}$ is involved in (pairs of) Shilnikov homoclinic orbits, EtoP connections, and possibly other global bifurcations. To this end, we extend the definition of (finite) symbol sequences of homoclinic orbits from the previous section to generic parameter points, where $W^u_+(\mathbf{0})$ makes excursions around p^+ and p^- infinitely many times, which leads to infinite symbol sequences.

We find it helpful to define such (infinite) sequences with the symbols $+$ and $-$. More specifically, for a generic point in the parameter plane, we define the kneading sequence

$$S(\rho, \mu) = S := (+\, s_1\, s_2\, \dots) \in \Sigma \subseteq \{+, -\}^{\mathbb{N}}, \tag{4}$$

with $s_i = +$ when the ith extremum in x of $W^u_+(\mathbf{0})$ is a positive maximum in x and $s_i = -$ if it is a negative minimum. As before, because of the symmetry of system (1), one could equivalently consider the kneading sequence of the branch $W^u_-(\mathbf{0})$, with the opposite symbols.

The kneading sequence is finite at (nongeneric) points of the (ρ, μ)-plane, for example, where a global homoclinic bifurcation exists; it is then given by the corresponding finite symbol sequence defined in Se. 3, where `r` is replaced by $+$ and `l` by $-$. We find it useful to maintain this difference in notation between infinitely long kneading sequences of $W^u_+(\mathbf{0})$ and finite symbol sequences at global bifurcations, chiefly because any kneading diagram in the parameter plane is necessarily only computed up to a finite number of symbols. We emphasize that the sweeping technique does not compute global bifurcations themselves. However, it is a suitable method to identify where they are approximately located, namely, at corresponding changes of the kneading sequence. Once we identify a certain global bifurcation in this way, we are able to compute the corresponding curve with Lin's method as a solution to a suitably posed boundary value problem [29].

We use the software package TIDES [1] to compute $W^u_+(\mathbf{0})$ to high-precision and find the relevant maxima and minima of x. Taking sufficiently long pieces of the trajectory generated by $W^u_+(\mathbf{0})$ allows us to determine a sufficiently large number of these extrema. In practice, we ensure that we are able to identify up to twenty positive maxima and/or negative minima. This method is efficient because, in principle, it is not necessary to have very long kneading sequences to get a suitably fine distinction between different topological cases. As an illustrative example, Fig. 10 shows four short trajectories generated by $W^u_+(\mathbf{0})$ for fixed $\mu = 2.5$ and different values of ρ, computed until the corresponding kneading sequences have three symbols. Since the first symbol in (4) is always $+$, the four cases in Fig. 10 cover all possibilities. Here, the top row shows $W^u_+(\mathbf{0})$ in projection onto the (x, y)-plane, and the bottom row its corresponding time series of x. Specifically, in panels (a1) and (a2), $W^u_+(\mathbf{0})$ has three consecutive positive maxima, yielding $S = (+ + + \dots)$; and in panels (b1) and (b2), it has two positive maxima and a negative minimum, yielding $S = (+ + - \dots)$. The change in the third symbol indicates that there must be a homoclinic bifurcation with symbol sequence $s =$ `rr` for an intermediate value of ρ. Similarly, the trajectories generated by $W^u_+(\mathbf{0})$ in Fig. 10 (c) and (d) have the kneading sequences $S = (+ - + \dots)$ and $S = (+ - - \dots)$, respectively, which indicates the presence in between of a homoclinic bifurcation with symbol sequence $s =$ `rl`. Moreover, there must be a homoclinic bifurcation with symbol sequence $s =$ `r` in between panels (b) and (c). This illustrates that two kneading sequences that differ from the i-th symbol are separated by a homoclinic bifurcation of level $i - 2$, with symbol sequence based on the first $i - 1$ symbols.

In order to visualize the kneading sequences in the (ρ, μ)-plane, we define the kneading invariant

$$K_n = K_n(S) = \sum_{i=0}^{n} s_i \frac{1}{2^{(i+1)}} \quad \text{of } S = (+\, s_1\, s_2 \dots), \tag{5}$$

computed up to $n{+}1$ symbols, which allows us to identify homoclinic bifurcations up to level $n{-}1$. Since $s_0 = +$, the kneading invariant K_n takes values in the interval $[0, 1]$. By construction, the

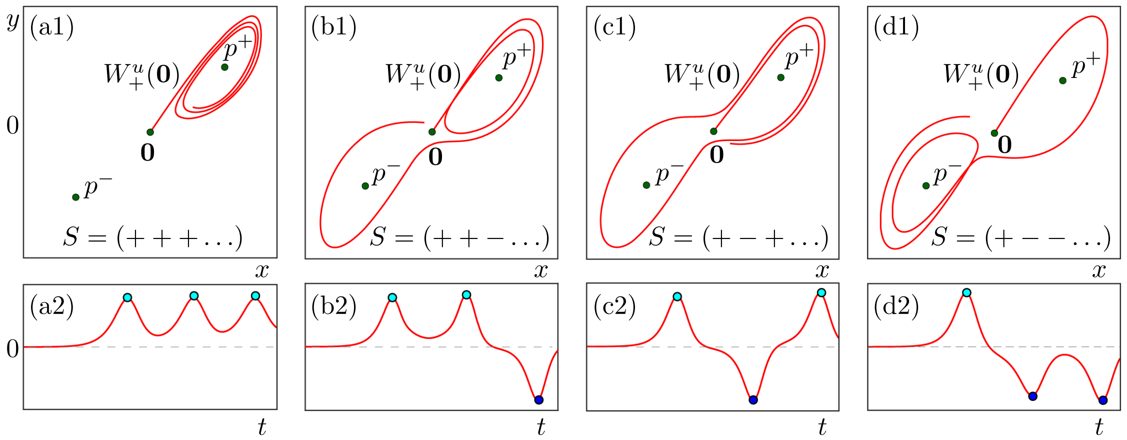

Figure 10: Short initial segment of the branch $W^u_+(0)$ (red curve) of (1) with $\mathbf{0}$ and $p^\pm$ (green dots) for fixed $\mu = 2.5$, and $\rho = 13$ (a), $\rho = 17$ (b), $\rho = 19$ (c), and $\rho = 24$ (d). Shown are the projections onto the (x, y)-plane (top) and the time series of x (bottom), where the positive maxima (cyan dots) and negative minima (blue dots) define the first three symbols in the respective kneading sequences S.

numbers K_n divide the interval $[0, 1]$ into 2^n subintervals of length 2^{-n}, each of which represents a different initial kneading sequence to which we assign a specific colour. We find it particularly useful to consider the division of the (ρ, μ)-plane by K_n for increasing n; we refer to this as the kneading diagram of K_n. In this way, we obtain images of increasingly deeper complexity, which allows us to identify more subregions in the (ρ, μ)-plane and associated global bifurcations bounding them.

We present in Fig. 11 the same bifurcation curves as those shown in Fig. 6, over the same parameter ranges, overlaid on the kneading diagrams of K_2 in panel (a) and K_4 in panel (b). Figure 11(a) shows that the (ρ, μ)-plane is now divided into five regions distinguished by four different colours. Their boundaries correspond to four homoclinic orbits up to level one. For a fixed value of $\mu = 2.5$, as in Fig. 10, we observe the same sequence of four different regions with three homoclinic orbits separating them. One of these is the primary homoclinic bifurcation curve $\mathrm{Hom}_{\texttt{r}}$ bounding regions with kneading sequences $S = (++-\dots)$ and $S = (+-+\dots)$.

Significantly, Fig. 11(a) already identifies additional curves of homoclinic bifurcation that we did not encounter in Fig. 6. First of all, we find that a second curve $\mathrm{Hom}_{\texttt{rl}}$, forms the upper boundary of the region with kneading sequence $S = (+--\dots)$. It is distinct from the curve $\mathrm{Hom}_{\texttt{rl}}$ we identified earlier, which forms the lower boundary of this region. As we continue this new curve $\mathrm{Hom}_{\texttt{rl}}$ in the direction of decreasing ρ, we find that it approaches and ends at the homoclinic explosion point $(\rho_{\texttt{r}}, 0)$. Secondly, the two regions with kneading sequences $S = (+++\dots)$ and $S = (++-\dots)$ are separated by the homoclinic bifurcation curve $\mathrm{Hom}_{\texttt{rr}}$. This global bifurcation lies above $\mathrm{Hom}_{\texttt{r}}$ and can also be continued to the homoclinic explosion point as $\mu \to 0$. It does not actually occur in the Lorenz system since there, $W^u_+(\mathbf{0})$ always immediately switches to perform at least one excursion around p^- before returning to $\mathbf{0}$.

Figure 12 displays these two newly found homoclinic orbits for fixed $\mu = 7$ in projections onto the (x, y)-plane (first column), the (z, w)-plane (second column), and as time series of x and w (third column). Panels (a1)–(a4) show $\mathrm{Hom}_{\texttt{rl}}$ at $\rho \approx 65.4113$, and panels (b1)–(b4) show $\mathrm{Hom}_{\texttt{rr}}$ at $\rho \approx 31.3119$. Comparing the first row of Fig. 12 with Fig. 7(a1) confirms that both homoclinic orbits, indeed, have the same symbol sequence $s = \texttt{rl}$ even though they belong to separate curves in the (ρ, μ)-plane. Note in Fig. 12 that it is not entirely possible to appreciate the 'excursions around' p^+ and p^- from the projections onto the (x, y) and (z, w)-planes; however, the kneading sequence is identified reliably from the respective maxima and

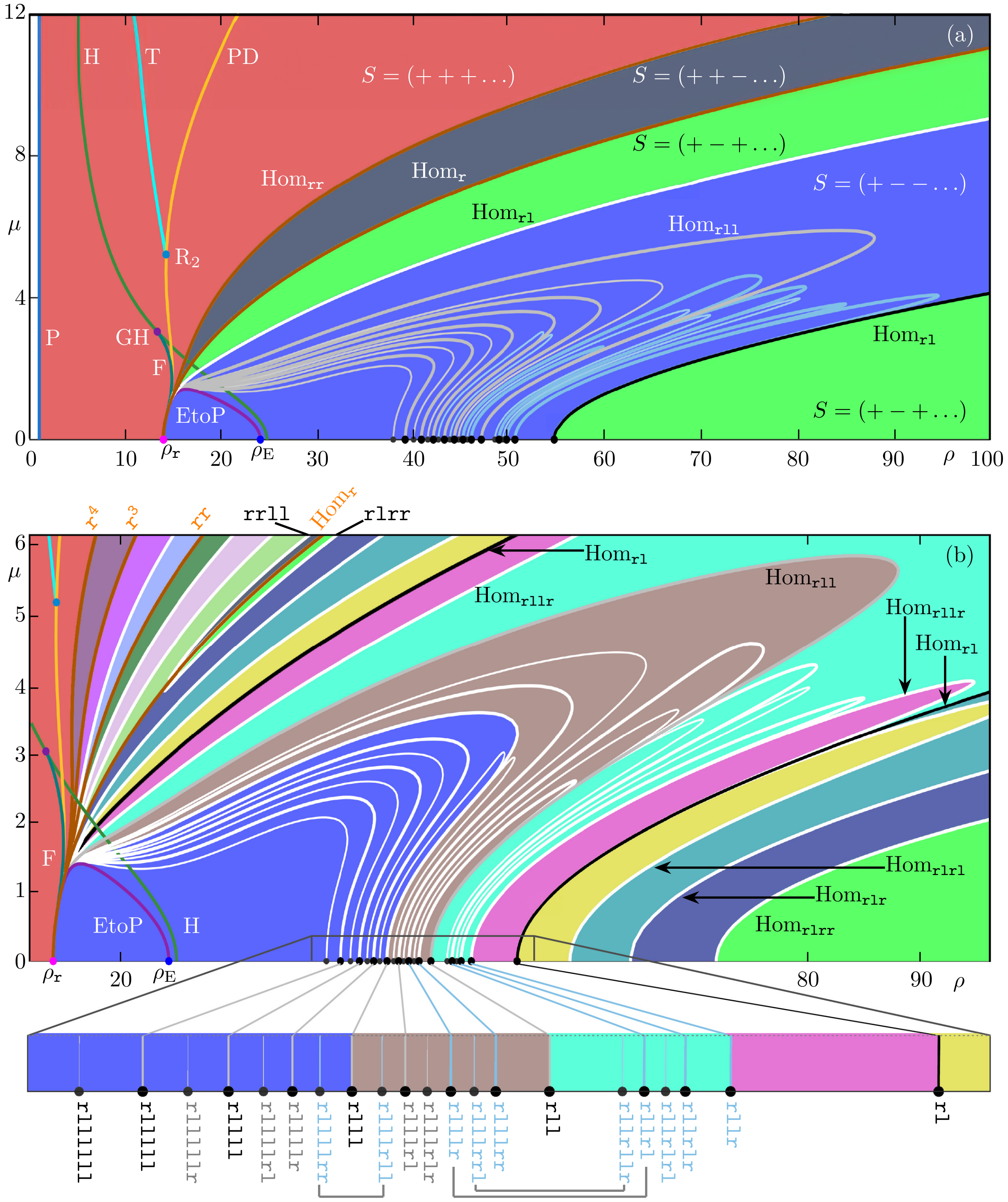

Figure 11: Colouring of the panels of Fig. 6 by the kneading invariants K_2 in panel (a) and K_4 in panel (b); also shown are several additional curves Hom_s of secondary homoclinic bifurcation.

minima of the time series of x; in this way, we identified the new homoclinic orbit $\mathrm{Hom}_\mathtt{rr}$ which is shown in panels (b1)–(b4); here, the homoclinic orbit has two loops near p^+ and then closes up without going to the region with negative x.

Figure 11(b) presents the kneading diagram of K_4, which divides the (ρ, μ)-plane into regions distinguished by 16 distinct colours. The kneading invariant K_4 identifies the curves of secondary homoclinic bifurcation Hom_s up to level three as boundaries between regions of different colours.

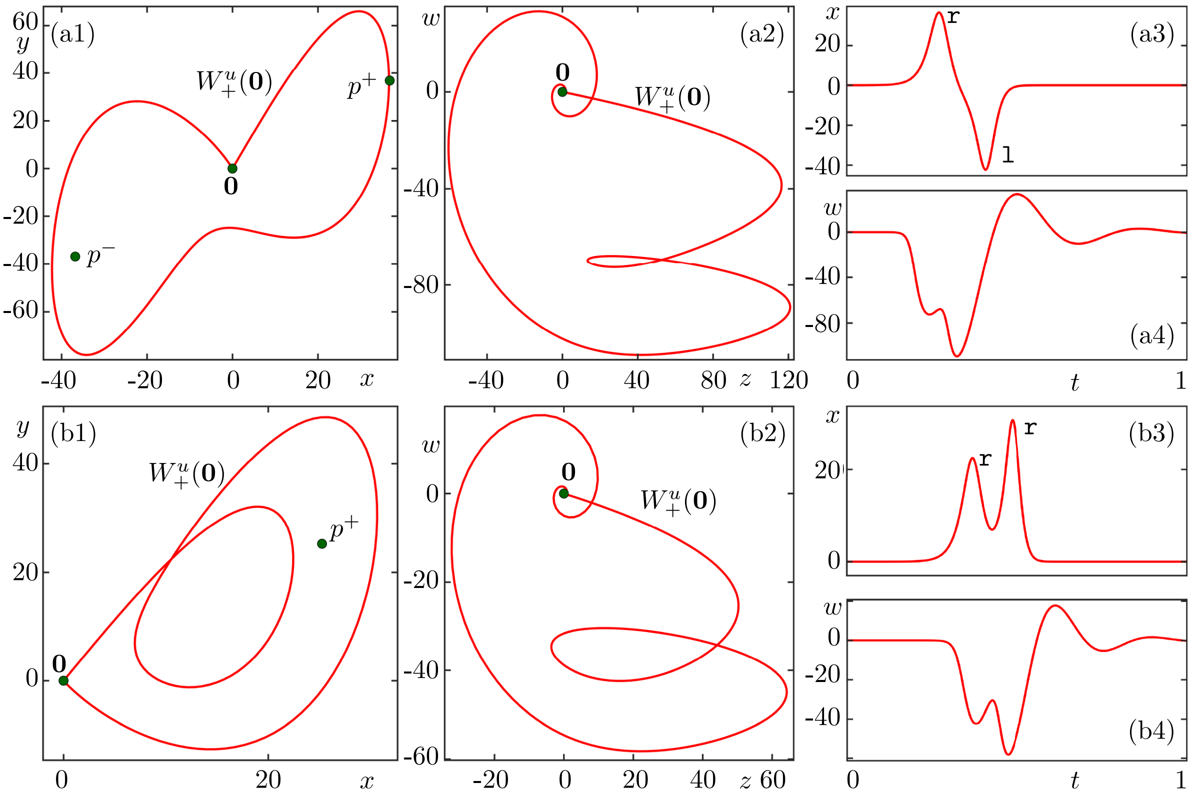

Figure 12: The secondary homoclinic orbits Hom_{s_i} with $s_1 = \texttt{rl}$ in panel (a) and $s_2 = \texttt{rr}$ in panel (b) formed by $W^u_+(\mathbf{0})$ for $\mu = 7$, shown with $\mathbf{0}$ and $p^\pm$ (green dots) in projections onto the (x, y)-plane (first column), onto the (z, w)-plane (second column), and as time series of x and w (third column). Here, $\rho \approx 65.4113$ in row (a) and $\rho \approx 31.3119$ in row (b).

This division is further illustrated in the enlargement at the bottom of the figure, where colour changes correspond to the secondary homoclinic orbits up to level three that we identified in the previous section. However, the kneading diagram of K_4 also suggests the existence of a number of additional global bifurcations. In particular, we found a second curve of a homoclinic orbit with symbol sequence $s = \texttt{rllr}$ in between the two curves $\mathrm{Hom}_{\texttt{rl}}$. Moreover, the kneading diagram of K_4 reveals three new curves of global bifurcation below the lower curve $\mathrm{Hom}_{\texttt{rl}}$; from right to left, they correspond to symbol sequences $\texttt{rlrr}$, $\texttt{rlr}$, and $\texttt{rlrl}$. When continued towards lower μ, these curves end on the ρ-axis at values of ρ to the right of the homoclinic explosion point associated with symbol sequence $\texttt{rl}$. While it is known that additional homoclinic bifurcations occur at higher values of ρ (for example, see the list in [41, Appendix I]), the method applied in [15] did not detect homoclinic bifurcation curves to the right of $\mathrm{Hom}_{\texttt{rl}}$. The kneading diagram of K_4 identifies these homoclinic bifurcation curves below the lower curve $\mathrm{Hom}_{\texttt{rl}}$ and we find that they are paired with curves with identical symbol sequences that lie above the upper curve $\mathrm{Hom}_{\texttt{rl}}$. This pairing is evident in Fig. 11(b) from the recurring colour patterns in the kneading diagram of K_4, which also highlights the primary homoclinic bifurcation curve $\mathrm{Hom}_{\texttt{r}}$ as the upper boundary for this pairing phenomenon.

At first glance, all curves of homoclinic bifurcation that lie above $\mathrm{Hom}_{\texttt{r}}$ in Fig. 11(b) appear to converge to the homoclinic explosion point $(\rho_{\texttt{r}}, 0)$ as $\mu \to 0$. Indeed, the homoclinic orbits Hom_s with symbol sequences $s = \texttt{r}^j$ behave this way: the curve $\mathrm{Hom}_{\texttt{rr}}$, was already identified in panel (a), and we also find those with $s = \texttt{rrr}$ and $s = \texttt{rrrr}$ in panel (b). These curves fan out further above and to the left of $\mathrm{Hom}_{\texttt{r}}$ for larger j. However, observe in Fig. 11(b) that the curves with symbol sequences $s_1 = \texttt{rlrr}$ and $s_2 = \texttt{rrll}$, only exist for larger values of μ. More

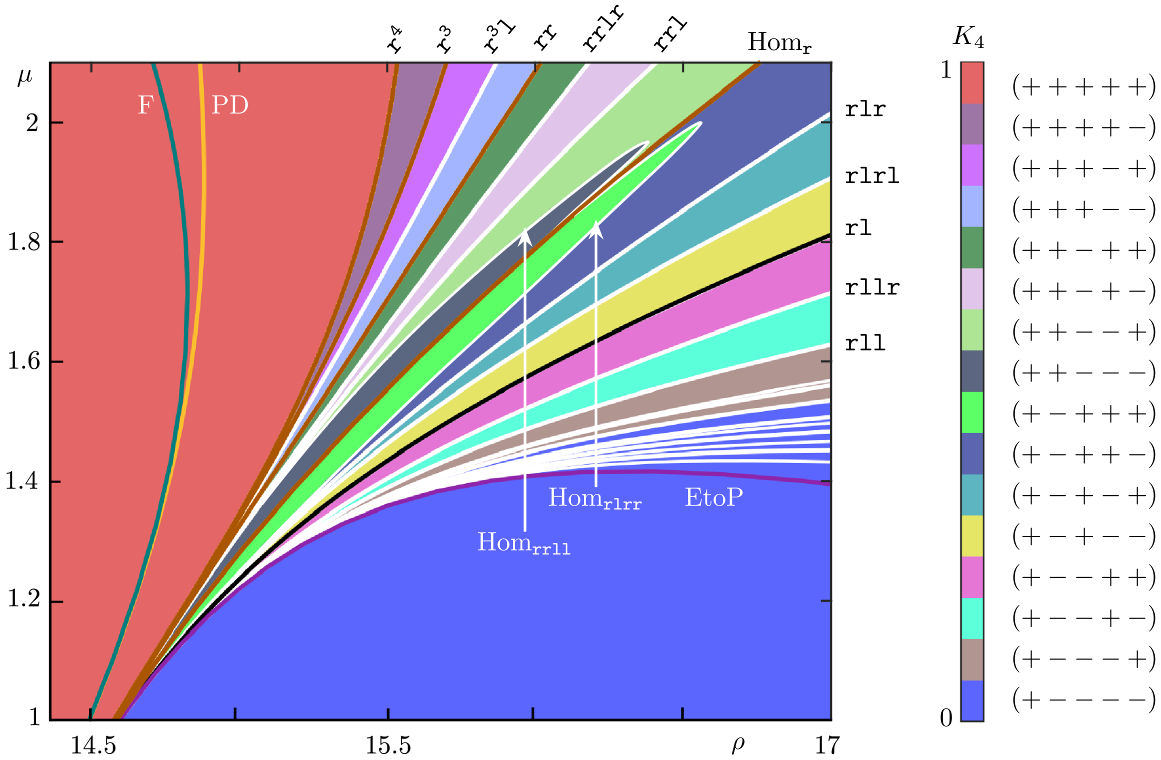

Figure 13: Enlargement of the kneading diagram of K_4 from Fig. 11; its kneading sequences are distinguished according to the colour bar.

precisely, when we continue these curves in the direction of decreasing μ, they do not converge to the homoclinic explosion point $(\rho_{\mathtt{r}}, 0)$ as $\mu \to 0$. Instead, these curves approach the primary homoclinic bifurcation $\mathrm{Hom}_{\mathtt{r}}$ from the right and left, respectively, reach minimum values of μ and of ρ, after which they turn around and follow $\mathrm{Hom}_{\mathtt{r}}$ closely towards large values of μ and ρ. This behaviour raises the question of whether these homoclinic orbits exist at lower values of μ, specifically, in the vicinity of the homoclinic explosion point $(\rho_{\mathtt{r}}, 0)$.

To address this question, we compute and display in Fig. 13 the kneading diagram of K_4 in an enlarged view near the homoclinic explosion point $(\rho_{\mathtt{r}}, 0)$ in the (ρ, μ)-plane. In fact, we identify here another pair of branches of homoclinic orbits with symbol sequences $s_1 = \mathtt{rlrr}$ and $s_2 = \mathtt{rrll}$, which are different from those previously found. These two curves emerge from the homoclinic explosion point and exhibit behaviour complementary to their counterparts (with the same symbol sequences at larger μ values): they approach the primary homoclinic bifurcation curve $\mathrm{Hom}_{\mathtt{r}}$ from the right and left, respectively, reach maximum values of μ and of ρ, and then turn back to $(\rho_{\mathtt{r}}, 0)$ along $\mathrm{Hom}_{\mathtt{r}}$ as $\mu \to 0$. From this, we conclude that these curves of secondary homoclinic orbits with symbol sequences s_1 and s_2 exist both in the vicinity of $(\rho_{\mathtt{r}}, 0)$ as well as for large values of μ and ρ; however, the respective curves are not connected, rather, they have 'finger' shapes, as can be seen in Fig. 13.

Figure 13 also further illustrates the behaviour of the curves of homoclinic orbits with symbol sequences of the form $s = \mathtt{r}^j$. Specifically, the curve corresponding to the largest value of j appears to establish a left boundary for all other homoclinic orbits with symbol sequences up to level $j - 2$.

Figure 11 and Fig. 13 seem to suggest that all curves of homoclinic bifurcation accumulate on some limiting curve on the left. In Fig. 14, we present the kneading diagram of K_9 near $(\rho_{\mathtt{r}}, 0)$ over a larger range of the (ρ, μ)-plane; compare with Fig. 11 and Fig. 13. Overlaid in Fig. 14 are the computed curves (brown) Hom_s with $s = \mathtt{r}^j$ for $1 \leq j \leq 9$. Figure 14 shows that there

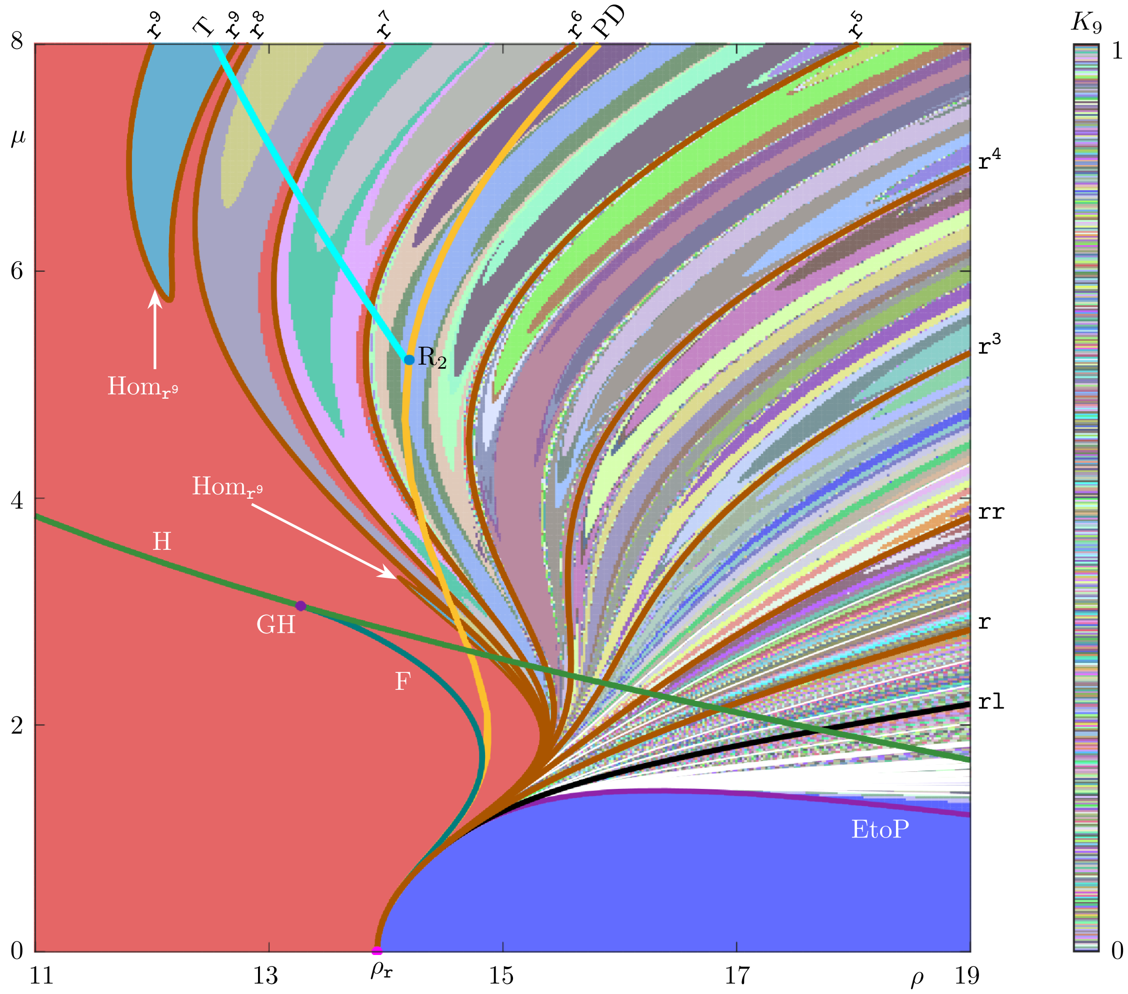

Figure 14: Kneading diagram of K_9 near $(\rho_{\mathtt{r}}, 0)$ with the curves of homoclinic bifurcation with symbol sequences of the form $s = \mathtt{r}^j$ with $1 \leq j \leq 9$ (brown). Values of K_9 are distinguished according to the colour bar.

are additional curves of homoclinic bifurcation to the left of the curve $\mathrm{Hom}_{\mathtt{rrrr}}$; approximately, for $\mu < 2.7$, all these curves seem to accumulate to the right of the curve PD. However, when μ is slightly larger than 2.7, this is no longer the case and the curves with symbol sequences $s = \mathtt{r}^j$ extend to the left of the curve PD, and also even beyond the curve T of torus bifurcation; compare with Fig. 11. The curves of homoclinic bifurcation with symbol sequences $s = \mathtt{r}^j$ with $1 \leq j \leq 8$ originate from the homoclinic explosion point $(\rho_{\mathtt{r}}, 0)$ and can be continued without limit for increasing ρ and μ. However, for $j = 9$, we observe a change: the curve $\mathrm{Hom}_{\mathtt{r}^9}$ splits into a pair of fingers, one finger emerging from the homoclinic explosion point $(\rho_{\mathtt{r}}, 0)$, and another from large values of ρ and μ.

Note the many changes in colour of the kneading diagram of K_9 between the specific curves of homoclinic bifurcation. They indicate the presence of additional homoclinic bifurcation curves with similar fingers, which we did not individually compute. Our findings suggest that many curves of homoclinic orbits exist in the vicinity of the homoclinic explosion point $(\rho_{\mathtt{r}}, 0)$, but not all of these extend to infinity in the (ρ, μ)-plane. On the other hand, it appears that the disjoint curves with the same symbol sequences also exist for sufficiently large values of ρ and μ.

5 Compactification of the parameter plane

We now investigate the global bifurcations for near-infinite values of ρ and μ in the parameter plane. For this purpose, we compactify the first quadrant of the (ρ, μ)-plane to a quarter sector of the unit disk D, often referred to as the (quarter) Poincaré disk, by introducing the transformation $P : \mathbb{R}^2 \to D$ given by

$$P(\rho, \mu) = (\tilde{\rho}, \tilde{\mu}) = \left(\frac{\rho}{R + \sqrt{R^2 + \rho^2 + (a\mu)^2}}, \frac{a\mu}{R + \sqrt{R^2 + \rho^2 + (a\mu)^2}} \right). \tag{6}$$

Here $R > 0$ and $a > 0$ are parameters that can be chosen to enhance the visibility of certain parts of the (ρ, μ)-plane. Specifically, we set $R = 30$ and $a = 4$ to position the parameter region near $(\rho^*, \mu^*) = (25, 7)$, where the wild chaotic attractor of (1) was observed in [23], near the centre of the compactified quarter disk, at $(\tilde{\rho}^*, \tilde{\mu}^*) = P(\rho^*, \mu^*) \approx (0.3202,\ 0.3587)$. Note that the (quarter) unit circle bounding D represents directions of escape to infinity in the (ρ, μ)-plane.

Figure 15 illustrates this compactification to the quarter disk by showing the bifurcation curves from Fig. 11(b) with the kneading diagram of K_4. Overlaid are all curves of homoclinic bifurcation up to level three, which we identified and computed directly in the compactified quarter disk. Indeed, the benefit of the compactification (6) goes beyond providing a global visualization of the parameter space; it allows us to detect all homoclinic bifurcation curves of system (1) up to a certain level. Observe that the bifurcation curves P, H, and T converge to the point $(\tilde{\rho}, \tilde{\mu}) = (0, 1)$, which corresponds to a limiting vertical slope in the (ρ, μ)-plane. This behaviour was already known from the analytical expressions of the pitchfork and Hopf bifurcations, but it was not previously observed for the torus bifurcation. In contrast, the bifurcation curve PD and several other curves of homoclinic bifurcation converge to the point $(\tilde{\rho}, \tilde{\mu}) = (1, 0)$, indicating a limiting horizontal slope in the (ρ, μ)-plane.

Figure 15 features several new curves of secondary homoclinic bifurcation. For instance, two curves with symbol sequence `rlr` were already identified in Fig. 11(b) and Fig. 13, yet the kneading diagram of K_4 in the compactified parameter disk reveals a third curve with the same symbol sequence. This curve emerges from $(\tilde{\rho}, \tilde{\mu}) \approx (0.7871, 0)$ and ends at $(\tilde{\rho}, \tilde{\mu}) = (1, 0)$. Another example is an additional curve of secondary homoclinic bifurcation with symbol sequence `rlrl` that acts as the boundary of a separate region of the kneading diagram of K_4; its endpoints are $(\tilde{\rho}, \tilde{\mu}) \approx (0.8118, 0)$ and $(\tilde{\rho}, \tilde{\mu}) \approx (0.8745, 0)$. Likewise, we observe a new curve Hom_s with symbol sequence `rlrr` with endpoints $(\tilde{\rho}, \tilde{\mu}) \approx (0.6664, 0)$ and $(\tilde{\rho}, \tilde{\mu}) \approx (0.7609, 0)$. The compactified parameter disk D also reveals extra regions and associated curves of homoclinic bifurcation 'at infinity', acting as counterparts to those that emanate from and return to the homoclinic explosion point $(\tilde{\rho}, \tilde{\mu}) = (\tilde{\rho}_{\mathtt{r}}, 0)$. An example is an additional curve $\mathrm{Hom}_{\mathtt{rll}}$ near the point $(\tilde{\rho}, \tilde{\mu}) = (1, 0)$, which serves as a counterpart to the one shown in Fig. 11.

5.1 Compactified kneading diagram of K_9

Figure 15 already provides global insights from the picture of the bifurcation structure of system (1) at the level of K_4. In particular, it suggests that the point $(\tilde{\rho}, \tilde{\mu}) = (1, 0)$ is another organizing centre 'at infinity', similar to the homoclinic explosion point $(\tilde{\rho}, \tilde{\mu}) = (\tilde{\rho}_{\mathtt{r}}, 0)$. To investigate this further, we show in Fig. 16 the kneading diagram of K_9 in the compactified quarter disk together with all identified curves of homoclinic bifurcation. It displays the different global properties with finer detail and increased complexity. We did not identify and continue all boundary curves between different regions of K_9, but their existence and symbol sequences can be inferred, as we showed for K_4 in Se. 4. As an additional feature, we also show the regions between consecutive curves of homoclinic bifurcation of the form $s = \mathtt{r}^j$ for $9 < j \leq 40$; they are represented by a colour gradient ranging from grey to light red. We compute and show these

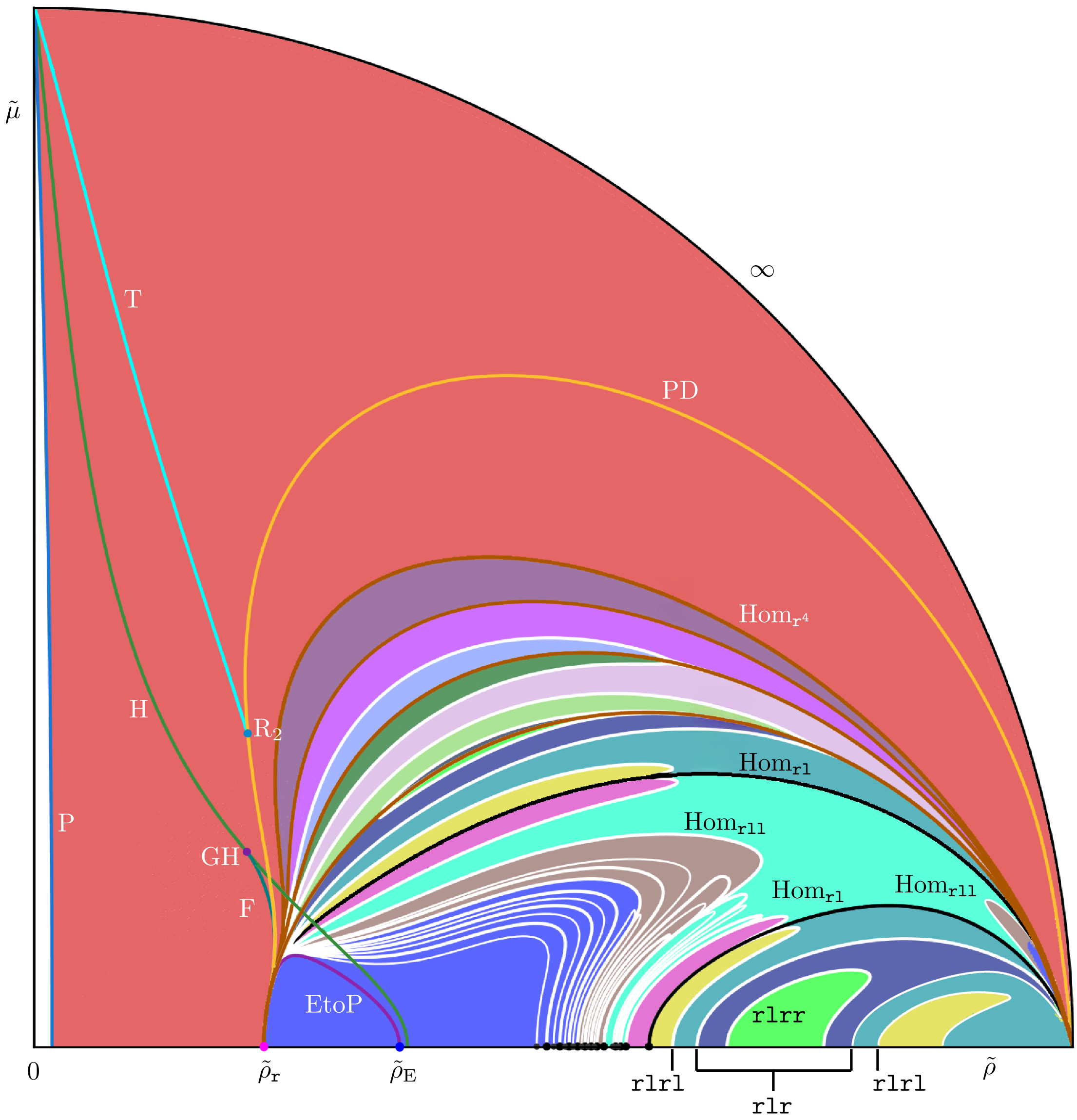

Figure 15: Two-parameter bifurcation diagram in the compactified quarter disk given by $(\tilde{\rho}, \tilde{\mu})$, coloured by the kneading diagram of K_4; compare with Fig. 11(b) and see Fig. 13 for the colour bar.

regions because the homoclinic orbits of this form act as upper boundaries for the respective kneading diagrams K_j. Figure 16 suggests that the pattern of homoclinic orbits extends all the way to infinity without an apparent upper boundary as the length of the symbol sequence increases. In the limit, these regions and homoclinic bifurcations appear to accumulate on the entire arc at infinity, staying to the right of the torus bifurcation curve T.

Observe in Fig. 16 how the curves of secondary homoclinic bifurcation that start and end on the $\tilde{\rho}$-axis are all well away from $\tilde{\rho} = 1$ and appear to be bounded by and accumulate on a (yet unknown) limiting curve or curves. This is reminiscent of boundaries for fingers-like regions in kneading diagrams discussed in [19, 20]. The 'accumulation curve(s)' of these fingers in Fig. 16 seems to bound the region of dense secondary homoclinic orbits on the right. The point $(\tilde{\rho}^*, \tilde{\mu}^*)$ where a wild pseudohyperbolic chaotic attractor was observed in [23] is located well within this region. The enlargement in the inset of Fig. 16 highlights the denseness of homoclinic bifurcations near this point.

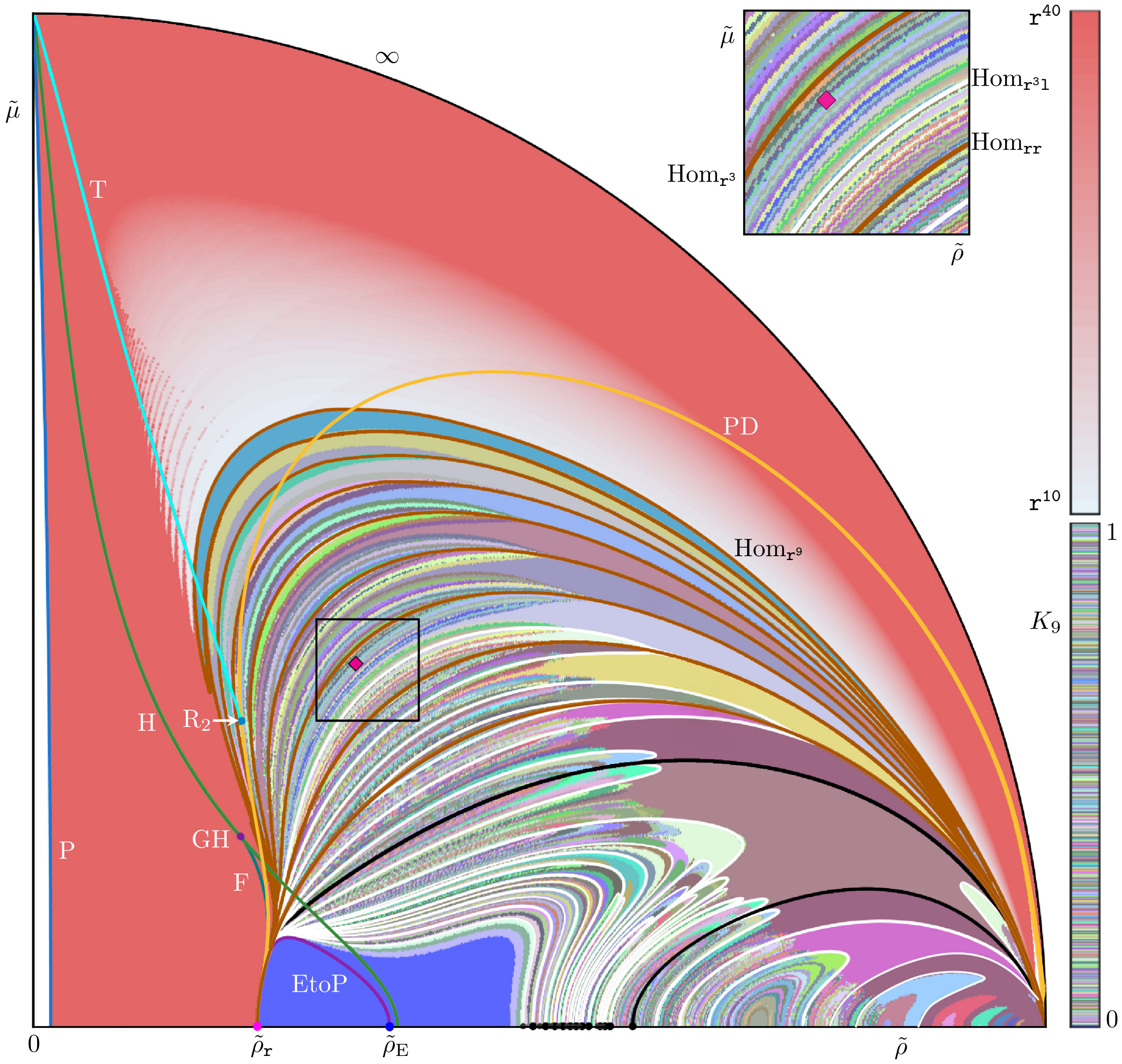

Figure 16: Two-parameter bifurcation diagram in the compactified quarter disk given by $(\tilde{\rho}, \tilde{\mu})$, coloured by the kneading diagram of K_9, as well as shades of red that indicate regions in between curves of homoclinic bifurcation with symbol sequences $\mathtt{r}^{n-1}$ and $\mathtt{r}^n$ up to $n = 40$. The magenta diamond marks the point $(\tilde{\rho}^*, \tilde{\mu}^*) \approx (0.3202, 0.3587)$ where the wild chaotic attractor was observed in [23], and the inset is an enlargement in the shown frame around it. Compare with Fig. 14.

We illustrate dense homoclinic bifurcations further in Fig. 17 with the kneading diagram of K_{11} in the uncompactified (ρ, μ)-plane over the same range as in Fig. 11(a); the point $(\rho^*, \mu^*) = (25, 7)$ from [23] is again marked. Observe that K_{11} in Fig. 17 shows a very fine structure in a large neighbourhood of (ρ^*, μ^*), providing clear numerical evidence for the 'wildness' in the (ρ, μ)-plane, complementing the corresponding images in the (ρ, σ)-plane in [23]. Notably, the region of dense homoclinic bifurcations is not restricted to a vicinity of the point (ρ^*, μ^*). Rather, it is quite large and appears to extend below the curve $\mathrm{Hom}_{\mathtt{r}}$ as well as to arbitrarily large values of μ, as we illustrated in Fig. 16.

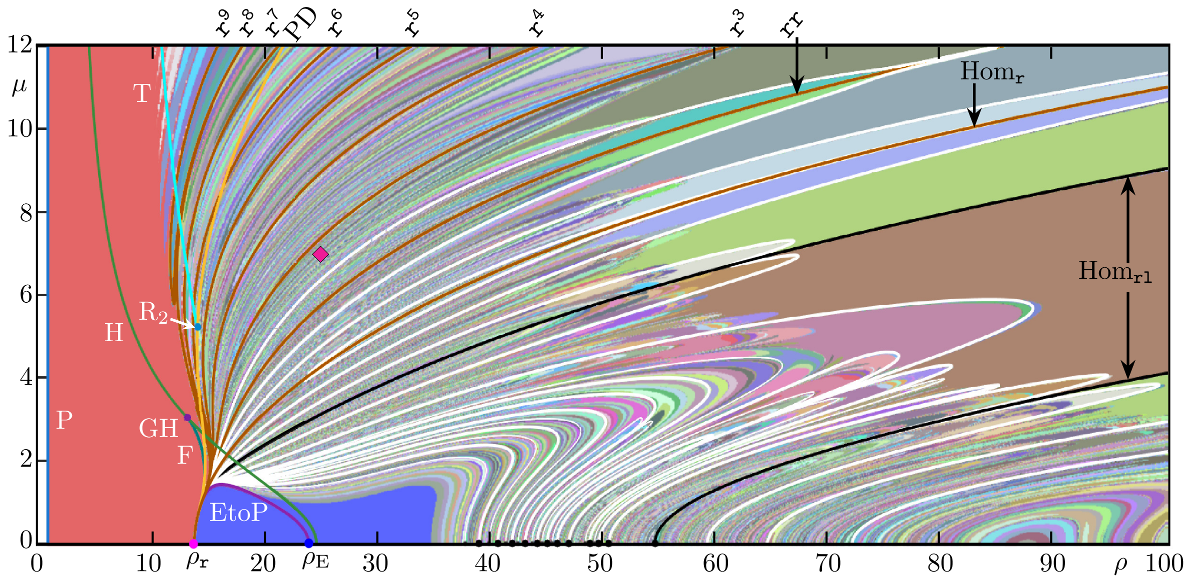

Figure 17: Kneading diagram of K_{11} in the (ρ, μ)-plane. The point $(\rho^*, \mu^*) = (25, 7)$ is marked with a magenta diamond. Compare with Fig. 11(a).

6 Lyapunov spectrum of the unstable manifold of the origin

The kneading diagrams from the previous sections provide insight into the topological structure and complexity of the accumulation and denseness of homoclinic orbits. However, they do not offer information about the nature of the corresponding invariant sets and/or attractors of system (1). To explore whether $W^u_+(\mathbf{0})$ approaches an equilibrium point, a periodic orbit, or a chaotic attractor (wild or not), we now examine how the associated Lyapunov spectrum varies across the (ρ, μ)-plane.

Since system (1) is a four-dimensional autonomous vector field, each trajectory has four Lyapunov exponents, denoted, in order, $\Lambda_4 \leq \Lambda_3 \leq \Lambda_2 \leq \Lambda_1$. At least one of these Lyapunov exponents is zero unless the trajectory converges to an equilibrium point. Moreover, the trace of the Jacobian matrix of system (1), given by $-(2\beta + \sigma + 1) = -49/3$ for $\sigma = 10$ and $\beta = 8/3$ as used here, is constant across the (ρ, μ)-plane. These two properties allow us to control the accuracy of our numerical computations when we compute the Lyapunov spectrum.

The negative trace implies that system (1) always has some attractor, to which the branch $W^u_+(\mathbf{0})$ converges generically; namely to:

(E) an attracting equilibrium if $\Lambda_1 < 0$,

(P) an attracting periodic orbit if $\Lambda_1 = 0$,

(C) a chaotic attractor (wild or not) if $\Lambda_1 > 0$.

The authors of [23] separate case (C) into *quasiattractors* and *pseudohyperbolic* attractors [3]. A quasiattractor is a 'regular' chaotic attractor, which is structurally unstable: a small perturbation of the system typically results in the appearance of a periodic attractor caused by the presence of so-called periodic windows in parameter space. In contrast, a *pseudohyperbolic* attractor exists robustly, and hence, the parameter space is free of periodic windows. As defined in [23, 22], we have the following cases of a chaotic attractor with $\Lambda_1 > 0$

(CQ) regular if $\Lambda_1 + \Lambda_2 + \Lambda_3 < 0$;

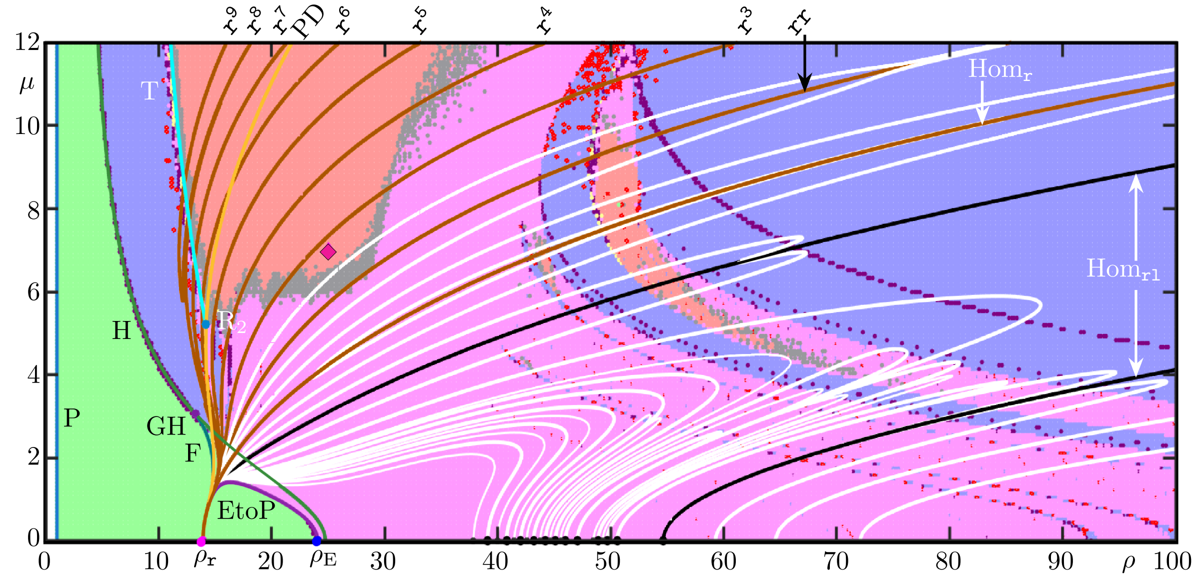

Figure 18: Colouring by the Lyapunov spectrum of $W^u_+(\mathbf{0})$ in the (ρ, μ)-plane. The regions are distinguished by the cases described in Table 3. Namely, (E) (green), (P) (blue), (CQ) (magenta) and (CP) (red). Additionally, the region of numerical uncertainty (B1) (purple) and (B2) (grey). Shown are also the bifurcation curves from Fig. 17 and the point (ρ^*, μ^*) (magenta diamond).

(CP) pseudohyperbolic if $\Lambda_1 + \Lambda_2 + \Lambda_3 > 0$.

Technically speaking, case (CP) implies that the chaotic attractor is pseudohyperbolic provided that certain conditions on the linearized dynamics are also met, which we do not verify here; see [23] for further details.

We compute the Lyapunov spectrum of $W^u_+(\mathbf{0})$ for points on a grid in the (ρ, μ)-plane with the method from [11]: we integrate system (1) together with its linearization up to a specified integration time; a GramSchmidt orthonormalization process is employed to control the Lyapunov vectors. Since any computation is subject to numerical tolerances, we introduce a small parameter $\varepsilon > 0$ and distinguish the asymptotic behaviour of $W^u_+(\mathbf{0})$ as summarized in Table 3. In particular, we also include borderline cases, denoted (B1) and (B2), which arise when the accuracy does not allow us to distinguish clearly between different attractor types.

Figure 18 shows the result of this calculation for a grid of 1000×300 parameter points in the (ρ, μ)-plane over the ranges $0 \leq \rho \leq 100$ and $0 \leq \mu \leq 12$; which is exactly the parameter region shown in Fig. 17. The first segment of $W^u_+(\mathbf{0})$ was obtained by starting from a point at a small distance from $\mathbf{0}$ along the unstable eigenvector $E^u(\mathbf{0})$ and integrating by using the standard Runge-Kutta fourth-order method over 300 units of time. A crucial issue in this computation is the choice of the tolerance parameter ε. We found that $\varepsilon = 0.08$ yields reliable results based on the criterion that the sum of the Lyapunov exponents is equal to the (constant) trace of the Jacobian to within 10^{-4} units. Although the value of ε may seem relatively large, it is consistent with those used in other numerical studies of Lyapunov exponents in the literature; see, for example, [8, 27, 5, 4, 46].

Observe in Fig. 18 that the region of attracting equilibria, as determined by criterion (E), is bounded by the curves P, H and F, as well as the curve EtoP on the other side of F. As soon as the curve H of Hopf bifurcation is crossed, the attractor is a periodic orbit according to criterion (P); as expected from theory, criterion (P) is satisfied effectively up to the curve T of torus bifurcation. Figure 18 reveals that criterion (P) is also satisfied in a second, large

case	criterion				attractor	color
(E)	$\Lambda_1 < -\varepsilon;$				equilibrium	green
(P)	$\lvert\Lambda_1\rvert < \varepsilon,$	$\Lambda_2 < -\varepsilon;$			periodic orbit	blue
(B1)	$\lvert\Lambda_1\rvert < \varepsilon,$	$\lvert\Lambda_2\rvert < \varepsilon,$	$\Lambda_3 < -\varepsilon;$		periodic—chaotic	purple
(CQ)	$\Lambda_1 > \varepsilon,$	$\lvert\Lambda_2\rvert < \varepsilon,$	$\Lambda_3 < -\varepsilon,$	$\Lambda_1 + \Lambda_2 + \Lambda_3 < -\varepsilon;$	chaotic regular	magenta
(B2)	$\Lambda_1 > \varepsilon,$	$\lvert\Lambda_2\rvert < \varepsilon,$	$\Lambda_3 < -\varepsilon,$	$\lvert\Lambda_1 + \Lambda_2 + \Lambda_3\rvert < \varepsilon;$	regular—pseudohyperbolic	grey
(CP)	$\Lambda_1 > \varepsilon,$	$\lvert\Lambda_2\rvert < \varepsilon,$	$\Lambda_3 < -\varepsilon,$	$\Lambda_1 + \Lambda_2 + \Lambda_3 > \varepsilon;$	chaotic pseudohyperbolic	red

Table 3: Classification criteria for the Lyapunov spectrum of $W^u_+(\mathbf{0})$.

region that is interrupted by a band of chaotic dynamics that satisfy criteria (CQ) or (CP). We are interested in the large 'primary' region that contains the point (ρ^*, μ^*) and satisfies criterion (CP), consistent with the results in [23]. It exists to the right of the curve T and above the boundary case (B2); the region satisfying criterion (CQ) is located below the boundary (B2) and extends all the way to the ρ-axis. Additionally, Fig. 18 shows a 'secondary' region where criterion (CP) also holds. It is bounded by regions with attracting periodic orbits and again separated from the region of regular chaotic dynamics by the borderline case (B2).

Figure 17 and Fig. 18 provide complementary yet distinct information. Figure 17 clearly suggests that the curves of secondary homoclinic bifurcation are dense near (ρ^*, μ^*). However, it is difficult to determine the extent or size of this region from this figure alone. When comparing with Fig. 18, it becomes clearer how far this region extends: approximately above the curve of secondary homoclinic bifurcation $\mathrm{Hom}_{\mathtt{rr}}$, to the right of the curve T and up to $\rho \approx 35$. Additionally, in the 'secondary' region where criterion (CP) is satisfied, the kneading diagram in Fig. 17 appears filled with curves of secondary homoclinic bifurcation, which may also indicate the presence of a wild pseudohyperbolic chaotic attractor there. While Fig. 17 suggests that homoclinic bifurcations are dense in many regions, Fig. 18 reveals that this does not generally imply the presence of a pseudohyperbolic attractor. This suggests that there are open regions in the (ρ, μ)-plane with wild hyperbolic (saddle) sets.

7 Conclusions and Outlook

We presented the global bifurcation structure in the two-parameter (ρ, μ)-plane of the four-dimensional Lorenz-like system (1). Building upon results for the Lorenz system from [15], we continued curves of global homoclinic bifurcation that emanate from the classic Lorenz system for $\mu = 0$. We found that all of these curves are bounded above by the primary homoclinic bifurcation $\mathrm{Hom}_{\mathtt{r}}$, and lie below the point (ρ^*, μ^*), where a wild pseudohyperbolic chaotic attractor was shown to exist [23].

We found additional global bifurcations that are intrinsic to the four-dimensional Lorenz-like system; we detected and continued them as curves in the (ρ, μ)-plane via kneading diagrams in combination with Lin's method [29]. Some of these curves also originate from the homoclinic explosion point $(\rho_{\mathtt{r}}, 0)$, while others emerge from a point at infinity or other homoclinic explosion points along the ρ-axis. In particular, these curves appear to be dense in a large region containing the point (ρ^*, μ^*), which is strong numerical evidence for the wild nature of the chaotic attractor at this parameter point.

We further analysed the system's attractors by computing the Lyapunov spectrum associated with the branch $W^u_+(\mathbf{0})$ of the one-dimensional unstable manifold of the origin. In this way, we identified different regions in terms of the Lyapunov spectrum, including the region containing the wild pseudohyperbolic attractor from [23]. We also found additional regions satisfying these conditions, suggesting that wild pseudohyperbolic attractors may arise in other parts of the (ρ, μ)-plane.

Our results suggest possible routes to wild chaos, and our approach is similar in spirit to that of [8, 19], where the computation of kneading invariants and Lyapunov spectra are employed to uncover the underlying geometry of complicated dynamics in two four-dimensional systems arising in photonics. We focused here on chaotic pseudohyperbolic attractors that exhibit robust homoclinic tangencies, which follow from the denseness of Shilnikov homoclinic orbits and classify them as wild [23, 37]. The robust presence of homoclinic tangencies implies the existence of heterodimensional cycles [32, 33, 34]. Thus far, we know of only one explicit example of a vector field with a heterodimensional cycle, namely, the so-called Atri model of intracellular calcium dynamics [47, 26]. In an initial investigation, we found periodic orbits with the appropriate indices (dimension of the unstable manifold), but the presence of heterodimensional cycles themselves in system (1) remains to be investigated. Their existence could act as a precursor to the emergence of a wild chaotic attractor—analogous to how the invariant set of a Smale horseshoe can become a chaotic attractor through certain bifurcations. This potential connection is interesting and offers a pathway to understanding the mechanisms through which wild chaotic attractors are created or destroyed.

Our work suggests another route to wild chaos, namely, involving the breakup of invariant tori with overlapping resonance tongues. We observed that this appears to be an ingredient in the transition to the main region containing the wild pseudohyperbolic chaotic attractor identified in [23]. Understanding the exact nature of this transition is a challenging task for future investigation.

Another interesting direction is to study the unfolding of the homoclinic explosion point $(\rho, \mu) = (\rho_{\mathbf{T}}, 0)$, which is richer in system (1) than in the Lorenz system. Equally interesting is the point of the Lorenz system in the limit where $\rho \to \infty$, which has been considered in [18, 38, 39, 41, 7]. In the four-dimensional system (1), it serves as a second organizing centre at $(\tilde{\rho}, \tilde{\mu}) = (1, 0)$ of the compactified parameter plane. Studying the dynamics near this point requires suitable changes of coordinates and blow-up techniques to capture the nearby dynamics. More broadly, the approach and computational methods developed in this work provide a framework that can be applied to other four-or higher-dimensional systems with the potential for new types of dynamics, including wild chaotic attractors or hyperbolic saddle sets.

Acknowledgements

The authors would like to thank Roberto Barrio, Rodrigues Bitha, Andrus Giraldo, and Dmitry Turaev for helpful discussions. This work has been supported by Royal Society Te Apārangi Marsden Fund grant #22-UOA-204.

References

[1] Abad A, Barrio R, Blesa F and Rodríguez M 2012 Algorithm 924: TIDES, a Taylor series integrator for differential equations *ACM Trans. Math. Softw.* **39** 1–28 doi:10.1145/2382585.2382590

[2] Afraimovich V S, Bykov V V and Shilnikov L P 1977 Origin and structure of the Lorenz attractor *Dokl. Akad. Nauk SSSR* **234** 336–39

[3] Afraimovich V S and Shilnikov L P 1983 Strange attractors and quasiattractors *Nonlinear Dynamics and Turbulence* (Interaction of mechanics and mathematics series) ed Barenblatt G I, Iooss G and Joseph D D (Boston: Pitman) pp 1–34

[4] Barrio R and Serrano S 2009 Bounds for the chaotic region in the Lorenz model *Phys. D Nonlinear Phenom.* **238** 1615–24 doi:10.1016/j.physd.2009.04.019

[5] Barrio R and Shilnikov A 2011 Parameter-sweeping techniques for temporal dynamics of neuronal systems: Case study of Hindmarsh-Rose model *J. Math. Neurosci.* **1** 6 doi:10.1186/2190-8567-1-6

[6] Barrio R, Shilnikov A and Shilnikov L P 2012 Kneadings, symbolic dynamics and painting Lorenz chaos *Int. J. Bifurc. Chaos* **22** 1230016 doi:10.1142/S0218127412300169

[7] Barrio R, Blesa F and Serrano S 2012 Behavior patterns in multiparametric dynamical systems: Lorenz model *Int. J. Bifurc. Chaos* **22** 1230019 doi:10.1142/S0218127412300194

[8] Bitha R D D, Giraldo A, Broderick N G R and Krauskopf B 2023 Bifurcation analysis of complex switching oscillations in a Kerr microring resonator *Phys. Rev. E* **108** 064204 doi:10.1103/PhysRevE.108.064204

[9] Bonatti C, Diaz L J and Viana M 2005 *Dynamics Beyond Uniform Hyperbolicity. A Global Geometric and Probabilistic Perspective* (Springer)

[10] Bykov V V and Shilnikov A 1992 On the boundaries of the domain of existence of the Lorenz attractor *Sel. Math. Sov.* **11** 375–82

[11] Christiansen F and Rugh H H 1997 Computing Lyapunov spectra with continuous Gram-Schmidt orthonormalization *Nonlinearity* **10** 1063 doi:10.1088/0951-7715/10/5/004

[12] Creaser J L, Krauskopf B and Osinga H M 2017 Finding first foliation tangencies in the Lorenz system *SIAM J. Appl. Dyn. Syst.* **16** 2127–64 doi:10.1137/17M1112716

[13] Doedel E J 1981 AUTO: A program for the automatic bifurcation analysis of autonomous systems *Congr. Numer* **30** 25–93

[14] Doedel E J 2007 AUTO-07p: Continuation and bifurcation software for ordinary differential equations with major contributions from Champneys A R, Fairgrieve T F, Kuznetsov Yu A, Oldeman B E, Paffenroth R C, Sandstede B, Wang X J and Zhang C (http://cmvl.cs.concordia.ca/auto/)

[15] Doedel E J, Krauskopf B and Osinga H M 2006 Global bifurcations of the Lorenz manifold *Nonlinearity* **19** 2947–72 doi:10.1088/0951-7715/19/12/013

[16] Doedel E J, Krauskopf B and Osinga H M 2011 Global invariant manifolds in the transition to preturbulence in the Lorenz system *Indag. Math.* **22** 222–40 doi:10.1016/j.indag.2011.10.007

[17] Doedel E J, Krauskopf B and Osinga H M 2015 Global organization of phase space in the transition to chaos in the Lorenz system *Nonlinearity* **28** R113 doi:10.1088/0951-7715/28/11/R113

[18] Dullin H R, Schmidt S, Richter P H and Grossmann S K 2007 Extended phase diagram of the Lorenz model *Int. J. Bifurc. Chaos* **17** 3013–33 doi:10.1142/S021812740701883X

[19] Giraldo A, Broderick N G R and Krauskopf B 2022 Chaotic switching in driven-dissipative Bose-Hubbard dimers: When a flip bifurcation meets a T-point in $\mathbb{R}^4$ *Discrete Contin. Dyn. Syst.* **27** 4023–75 doi:10.3934/dcdsb.2021217

[20] Giraldo A, Krauskopf B and Osinga H M 2018 Cascades of global bifurcations and chaos near a homoclinic flip bifurcation: A case study *SIAM J. Appl. Dyn. Syst.* **17** 2784–829 doi:10.1137/17M1149675

[21] Glendinning P and Sparrow C 1984 Local and global behavior near homoclinic orbits *J. Stat. Phys.* **35** 645–96 doi:10.1007/BF01010828

[22] Gonchenko A, Gonchenko S, Kazakov A and Kozlov A 2018 Elements of contemporary theory of dynamical chaos: A tutorial. Part I. Pseudohyperbolic attractors *Int. J. Bifurc. Chaos* **28** 1830036 doi:10.1142/S0218127418300367

[23] Gonchenko S, Kazakov A and Turaev D V 2021 Wild pseudohyperbolic attractor in a four dimensional Lorenz system *Nonlinearity* **34** 2018–47 doi:10.1088/1361-6544/abc794

[24] Guckenheimer J and Holmes P 2013 *Nonlinear Oscillations, Dynamical Systems, and Bifurcations of Vector Fields* (Springer Science & Business Media)

[25] Guckenheimer J and Williams R F 1979 Structural stability of Lorenz attractors *Publ. Math. IHÉS* **50** 59–72 doi:10.1007/BF02684769

[26] Hammerlindl A, Krauskopf B, Mason G and Osinga H M 2022 Determining the global manifold structure of a continuous-time heterodimensional cycle *J. Comput. Dyn.* **9** 393–419 doi:10.3934/jcd.2022008

[27] Jelleyman H and Osinga H M 2022 Matching geometric and expansion characteristics of wild chaotic attractors *Eur. Phys. J. Spec. Top.* **231** 403–12 doi:10.1140/epjs/s11734-022-00440-w

[28] Kaplan J L and Yorke J A 1979 Preturbulence: A regime observed in a fluid flow model of Lorenz *Commun. Math. Phys.* **67** 93–108 doi:10.1007/BF01221359

[29] Krauskopf B and Rieß T 2008 A Lin's method approach to finding and continuing heteroclinic connections involving periodic orbits *Nonlinearity* **21** 1655–90 doi:10.1088/0951-7715/21/8/001

[30] Krauskopf B, Osinga H M and Galan-Vioque J (eds) 2007 *Numerical Continuation Methods for Dynamical Systems: Path Following and Boundary Value Problems* Understanding Complex Systems (Springer)

[31] Kuznetsov Y A 2018 *Elements of Applied Bifurcation Theory* (Springer)

[32] Li D 2017 Homoclinic bifurcations that give rise to heterodimensional cycles near a saddle-focus equilibrium *Nonlinearity* **30** 173–206 ISSN 0951-7715, 1361-6544 doi:10.1088/1361-6544/30/1/173

[33] Li D and Turaev D V 2024 Persistence of heterodimensional cycles *Invent. Math.* **236** 1413–504 doi:10.1007/s00222-024-01255-3

[34] Li D, Li X, Shinohara K and Turaev D V 2024 Robust heterodimensional cycles in two-parameter unfolding of homoclinic tangencies *Nonlinearity* **37** 1–30 doi:10.1007/s11071-024-08358-0

[35] Lorenz E N 1963 Deterministic nonperiodic flows *J. Atmos. Sci.* **20** 130–41 doi:10.1175/1520-0469(1963)020<0130:DNF>2.0.CO;2

[36] Newhouse S E 1974 Diffeomorphisms with infinitely many sinks *Topology* **13** 9–18 doi:10.1016/0040-9383(74)90034-2

[37] Newhouse S E 1979 The abundance of wild hyperbolic sets and non-smooth stable sets for diffeomorphisms *Publ. Math. IHÉS* **50** 101–51 doi:10.1007/BF02684771

[38] Ovsyannikov I, Rademacher J D M, Welter R and Lu B Y 2023 Time averages and periodic attractors at high Rayleigh number for Lorenz-like models *J. Nonlinear Sci.* **33** 73 doi:10.1007/s00332-023-09933-x

[39] Robbins K A 1979 Periodic solutions and bifurcation structure at high R in the Lorenz model *SIAM J. Appl. Math.* **36** 457–72 doi:10.1137/0136035

[40] Shilnikov L P, Shilnikov A, Turaev D V and Chua L O 1998 *Methods of Qualitative Theory in Nonlinear Dynamics, Part 2* (*Nonlinear Science Series A* vol 5) (World Scientific)

[41] Sparrow C 1982 *The Lorenz Equations: Bifurcations, Chaos and Strange Attractors* (*Applied Mathematical Sciences* vol 41) (Springer)

[42] Tucker W 1999 The Lorenz attractor exists *C. R. Acad. Sci. Ser. I Math.* **328** 1197–202 doi:10.1016/S0764-4442(99)80439-X

[43] Turaev D V and Shilnikov L P 1998 An example of a wild strange attractor *Math Sb.* **189** 291–314 doi:10.1070/SM1998v189n02ABEH000300

[44] Turaev D V and Shilnikov L P 2008 Pseudohyperbolicity and the problem on periodic perturbations of Lorenz-type attractors *Dokl. Math.* **77** 17–21 ISSN 1531-8362 doi:10.1134/S1064562408010055

[45] Turaev D V 2025 A Geometric Model for Pseudohyperbolic Shilnikov Attractors *Regul. Chaot. Dyn.* **30** 174–87 doi:10.1134/S1560354725020029

[46] Wolf A, Swift J B, Swinney H L and Vastano J A 1985 Determining Lyapunov exponents from a time series *Phys. D Nonlinear Phenom.* **16** 285–317 ISSN 0167-2789 doi:10.1016/0167-2789(85)90011-9

[47] Wong N, Krauskopf B and Osinga H M 2025 Cascades of heterodimensional cycles via period doubling *Commun. Nonlinear Sci. Numer. Simul.* **140** 108328 doi:10.1016/j.cnsns.2024.108328

[48] Xing T, Barrio R and Shilnikov A 2014 Symbolic quest into homoclinic chaos *Int. J. Bifurc. Chaos* **24** 1440004 doi:10.1142/S0218127414400045